arXiv:1201.5339v3 [cond-mat.mes-hall] 2 May 2012

Coherent radial breathing like phonons in graphene nanoribbons

G. D. Sanders[1], A. R. T. Nugraha[2], R. Saito[2], C. J. Stanton[1]
[1]*Department of Physics, University of Florida, Box 118440, Gainesville, Florida 32611-8440, USA*
[2]*Department of Physics, Tohoku University, Sendai 980-8578, Japan*

(Dated: May 3, 2012)

We have developed a microscopic theory for the generation and detection of coherent phonons in armchair and zigzag graphene nanoribbons using an extended tight-binding model for the electronic states and a valence force field model for the phonons. The coherent phonon amplitudes satisfy a driven oscillator equation with the driving term depending on photoexcited carrier density. We examine the coherent phonon radial breathing like mode amplitudes as a function of excitation energies and nanoribbon types. For photoexcitation near the optical absorption edge the coherent phonon driving term for the radial breathing like mode is much larger for zigzag nanoribbons where transitions between localized edge states provide the dominant contribution to the coherent phonon driving term. Using an effective mass theory, we explain how the armchair nanoribbon width changes in response to laser excitation.

PACS numbers: 63.22.-m, 73.22.-f, 78.67.-n

I. INTRODUCTION

Excited state lattice vibrations in carbon nanotubes have been studied with coherent phonon (CP) spectroscopy.[1–5] Using CP spectroscopy with pulse shaping techniques, radial breathing mode (RBM) coherent phonons in chirality-specific semiconducting single-walled carbon nanotubes have been studied experimentally.[5–8] The CP signals are resonantly enhanced when the pump photon energy coincides with an exciton resonance, and provides information on the chirality-dependence of light absorption, phonon generation, and phonon-induced band structure modulation.

Recently we developed a microscopic theory for the generation and detection of coherent phonons in single-walled carbon nanotubes in CP spectroscopy experiments.[5–7] We used the Heisenberg equation to obtain a driven oscillator equation for the coherent phonon amplitudes and found that the driving function depends explicitly on the time-dependent photoexcited carrier distribution functions.[5] Comparing theory and experiment we find that our model predicts overall trends in the relative strength of the RBM coherent phonon signal both within and between different tube types.

In a followup paper we studied the chirality dependence of coherent phonon amplitudes in single-wall carbon nanotubes over a large range of chiralities using an effective mass approach.[9] By examining the k-dependent electron-phonon interaction in the effective mass approximation, we were able to explain why some nanotubes start their coherent RBM diameter oscillations by initially expanding while others start their RBM diameter oscillations by initially shrinking their diameters, a fact recently observed experimentally.[8] In many solids, lattices tend to expand when photoexcited by ultrafast laser pulses in accordance with the Franck-Condon principle. As pointed out in Ref. 9 this is not the case for RBM diameter oscillations in carbon nanotubes where the diameter can either expand or contract depending on the nanotube chirality and photoexcitation energy.

The electronics industry is exploring device technologies based on carbon nanotubes, graphene, and graphene nanoribbons (GNRs).[10] Field-effect transistors based on GNRs have been demonstrated[11] and it is now possible to fabricate GNRs with atomically precise widths using a number of methods.[12–17] An understanding of the electronic and transport properties of GNRs is essential in realizing device applications for GNRs.[18] In particular it is important for characterization and transport modeling to have a good understanding of the electron-phonon interaction and lattice vibrations in GNRs. It is hoped that coherent phonon spectroscopy will prove useful in characterizing graphene and graphene nanoribbons in addition to carbon nanotubes.

In this paper, we extend our coherent phonon theory to the case of unpassivated zigzag and armchair nanoribbons. In our model, we calculate electronic states for the π electrons in an extended tight binding model (ETB),[5,19] while the phonon modes are treated in a valence force field framework.[20,21] Details concerning the computation of electronic states and phonon modes can be found in Appendices A and B respectively. In our formalism, we incorporate the electron-phonon interaction,[22] the optical matrix elements,[23] and the interaction of carriers with a classical ultrafast laser pulse.[5] For simplicity, we neglect the many-body Coulomb interaction. In carbon nanotubes, we found that there were exactly four CP active phonon modes independent of the tube's chirality. The most easily observed CP active mode in nanotubes is the RBM, which has the lowest frequency. In zigzag and armchair nanoribbons, on the other hand, the rotational degree of freedom about the nanotube axis is lost and the number of CP active phonon modes in zigzag or armchair nanoribbons is equal to the number of AB carbon dimers in the nanoribbon translational unit cell. The most easily observed of these CP modes is the one with the lowest frequency, namely the radial breathing like mode (RBLM).

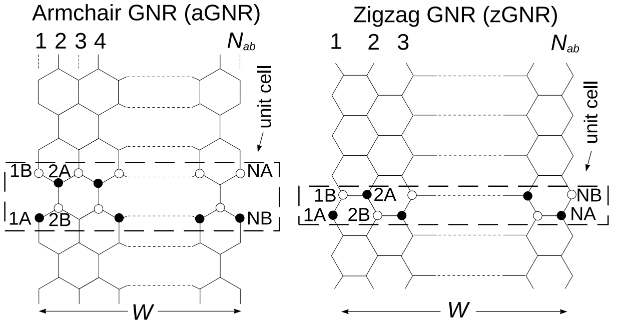

FIG. 1: Schematic diagram showing lattice structures and translational unit cells for armchair (aGNR) and zigzag (zGNR) graphene nanoribbons. The width of the nanoribbons is W.

II. THEORY

We consider two types of nanoribbon, namely zigzag and armchair ribbons.[24,25] The lattice structure for armchair and zigzag graphene nanoribbons is shown schematically in Fig. 1. These ribbons are denoted N_{ab} zGNR and N_{ab} aGNR respectively where N_{ab} is the number of AB carbon dimers in the translational unit cell. In zigzag ribbons, the length L of the translational unit cell is a and the width W of the ribbon is $(N_{ab}-1)\,\frac{\sqrt{3}}{2}a$ where $a = 2.49$ Å is the hexagonal lattice constant in graphene. In armchair ribbons, the translational unit cell length is $\sqrt{3}a$ and the ribbon width is $(N_{ab}-1)\,\frac{1}{2}a$. Note that in zigzag and armchair ribbons with the same number of atoms per unit cell, the area of the unit cells are equal. Note that we do not allow for the relaxation of the bond lengths at the surfaces.

A. Coherent phonon generation

In coherent phonon spectroscopy, the coherent phonon modes that are usually excited are the modes with wavevector $q = 0$ whose amplitudes satisfy a driven oscillator equation

$$\frac{\partial^2 Q_m(t)}{\partial t^2} + \omega_m^2 Q_m(t) = S_m(t), \tag{1}$$

where m denotes the phonon mode and $\omega_m \equiv \omega_m(q=0)$ is the frequency of phonon mode m at $q = 0$. There is no damping term in Eq. (1) since anharmonic terms in the electron-phonon Hamiltonian are neglected. We solve the driven oscillator equation subject to the initial conditions $Q_m(0) = \dot{Q}_m(0) = 0$. The driving function $S_m(t)$ is given by

$$S_m(t) = -\frac{2\omega_m}{\hbar} \sum_{nk} M_n^m(k) \left(f_n(k,t) - f_n^0(k) \right). \tag{2}$$

where $f_n(k,t)$ are the time-dependent electron distribution functions and $f_n^0(k)$ are the initial equilibrium electron distribution functions. Here n labels the electronic state and k is the electron wavevector. The electron-phonon matrix element $M_n^m(k) \equiv M_{nk;nk}^{m0}$ where $M_{n'k';nk}^{mq}$ is the deformation potential electron-phonon matrix element in our ETB model. Details concerning calculation of this matrix element can be found in Appendix C.

The driving function $S_m(t)$ depends on the photoexcited electron distribution functions which can be calculated in the Boltzmann equation formalism taking photogeneration and relaxation effects into account. In CP spectroscopy, an ultrafast laser pulse generates electron-hole pairs on a time scale short in comparison with the coherent phonon period. The observed CP signal is proportional to the power spectrum of $Q_m(t)$. For simplicity we ignore relaxation effects and retain only the rapidly varying photogeneration term in the Boltzmann equation. This model works best when the carrier relaxation time is greater than the coherent phonon period. The ultrafast pump pulse gives an impulsive kick to $Q_m(t)$ setting the coherent phonon oscillations in motion. The subsequent slow relaxation of $S_m(t)$ shifts the coordinate about which $Q_m(t)$ oscillates but the coherent phonon oscillator is able to follow this shift adiabatically with negligible change in the oscillation amplitude and the corresponding power spectrum at the oscillation frequency. Thus neglecting carrier relaxation has a negligible effect on the computed CP signal.

The photogeneration rate is obtained from Fermi's golden rule and the equation of motion for the distribution functions on time scales short in comparison to the relaxation time is

$$\frac{\partial f_n(k)}{\partial t} = \frac{8\pi^2 e^2\ u(t)}{\hbar\ n_g^2\ (\hbar\omega)^2} \left(\frac{\hbar^2}{m_0}\right) \sum_{n'} |P_{nn'}(k)|^2 \times \Big(f_{n'}(k,t) - f_n(k,t) \Big)\ \delta\Big(\Delta E_{nn'}(k) - \hbar\omega \Big), \tag{3}$$

where $\Delta E_{nn'}(k) = |E_n(k) - E_{n'}(k)|$ are the k dependent transition energies, $\hbar\omega$ is the pump energy, $u(t)$ is the time-dependent energy density of the pump pulse, e is the electron charge, m_0 is the free electron mass, and n_g is the index of refraction in the surrounding medium. The pump energy density $u(t)$ is related to the fluence by $F = \int dt\ u(t)\ (c/n_g)$. The pump energy density is taken to be a Gaussian with an intensity full width at half maximum (FWHM) of τ_p which we define as the pump duration. The optical dipole matrix element is given by

$$P_{nn'}(k) = -\frac{i\hbar}{\sqrt{2m_0}}\ \hat{\epsilon} \cdot \int d\mathbf{r}\ \psi_{nk}^*(\mathbf{r})\ \nabla \psi_{n'k}(\mathbf{r}), \tag{4}$$

where $\hat{\epsilon}$ is the complex electric polarization vector of unit length and $\psi_{nk}(\mathbf{r})$ are the π electron tight-binding wavefunctions defined in Appendix A. With the aid of the π orbital expansions of the electron wavefunctions we can evaluate the optical dipole matrix element in Eq. (4) analytically. To account for spectral broadening of the laser pulses we replace the delta function in Eq. (3) with a

Lorentzian lineshape[26]

$$\delta(\Delta E - \hbar\omega) \to \frac{\Gamma_p/(2\pi)}{(\Delta E - \hbar\omega)^2 + (\Gamma_p/2)^2}, \qquad (5)$$

where Γ_p is the FWHM spectral linewidth of the pump pulse.

In addition to the photogeneration rate, there are also carrier relaxation effects to consider. In Ref. 27 Dawlaty *et al.* measured carrier relaxation times in photoexcited graphene using pump-probe spectroscopy and found two relaxation time scales for relaxation of photogenerated carriers. An initial fast relaxation transient with a relaxation time ranging from 70 to 120 fs is followed by a slower relaxation with a relaxation time ranging from 400 to 1700 fs. These effects can be modeled in a phenomenological relaxation time approximation which adds a term to the photogeneration rate in Eq. (3) of the form

$$\left(\frac{\partial f_n(k)}{\partial t}\right)_{\text{relax}} = -\left(\frac{f_n(k,t) - f_n^0(k)}{\tau_r}\right) \qquad (6)$$

where τ_r is the phenomenological relaxation time and $f_n^0(k)$ are the initial carrier distribution functions in thermal equilibrium.

In our tight-binding model we only include π bands. The σ bands in graphene have a direct gap at the Γ point of around 6 eV.[20] In nanoribbons the σ band direct gap will be even larger due to quantum confinement effects. The laser pulses discussed in this work are restricted to photon energies $\hbar\omega \leq 5$ eV so we need not consider coherent phonon generation due to photoexcited carriers from the σ bands.

From the coherent phonon amplitudes, the time-dependent macroscopic displacements of each carbon atom in the nanoribbon are given by

$$\mathbf{U}_{sj}^{l}(t) = \frac{\hbar}{\sqrt{2\rho L_\Omega}} \sum_m \frac{\hat{\mathbf{e}}_{sj}^m}{\sqrt{\hbar\omega_m}}\, Q_m(t) \qquad (7)$$

where $\hat{\mathbf{e}}_{sj}^m \equiv \hat{\mathbf{e}}_{sj}^m(q=0)$ is defined in Appendix B.

B. Coherent phonon detection

In coherent phonon spectroscopy a probe pulse is used to measure the time-varying absorption coefficient of the nanoribbon. The time-dependent absorption coefficient is given by[26,28]

$$\alpha(\hbar\omega, t) = \frac{\hbar\omega}{n_g \hbar c}\, \varepsilon_2(\hbar\omega, t), \qquad (8)$$

where $\varepsilon_2(\hbar\omega, t)$ is the imaginary part of the time-dependent dielectric function evaluated at the probe photon energy $\hbar\omega$.

The imaginary part of the nanoribbon dielectric function is obtained from Fermi's golden rule

$$\varepsilon_2(\hbar\omega) = \frac{8\pi^2 e^2}{W L_z (\hbar\omega)^2} \left(\frac{\hbar^2}{m_0}\right) \sum_{nn'} \int \frac{dk}{\pi}\, |P_{nn'}(k)|^2 \times \\ \Big(f_n(k) - f_{n'}(k)\Big)\, \delta\Big(E_{n'}(k) - E_n(k) - \hbar\omega\Big), \qquad (9)$$

where W is the nanoribbon width and $L_z = 3.4\,\text{Å}$ is the nanoribbon thickness taken to be the interlayer distance in graphite. We replace the delta function in Eq. (9) with a broadened Lorentzian spectral lineshape with a FWHM of Γ_s. The distribution function $f_n(k)$ and bandstructure $E_n(k)$ are time-dependent. The time-dependence of $f_n(k)$ comes from the photogeneration of carriers described by the Boltzmann carrier dynamics and the time-dependence of $E_n(k)$ comes from variations in the carbon-carbon bond lengths due to the macroscopic coherent phonon induced atomic displacements in Eq. (7). This time-dependent deformation of the nanoribbon bond lengths alters the tight-binding Hamiltonian and overlap matrix elements in the extended tight-binding model.[5] Note that to first order in the lattice displacements the energies $E_n(k)$ vary with time while the tight-binding wavefunctions and optical matrix elements $P_{nn'}(k)$ do not.

In coherent phonon spectroscopy, excitation of coherent phonons by the pump modulates the optical properties of the nanoribbons giving rise to a transient differential transmission signal. In our model we take the theoretical CP signal to be proportional to the power spectrum of the transient differential transmission after background subtraction. We compute the power spectrum using the Lomb periodogram algorithm described in Ref. 29.

III. ZIGZAG NANORIBBON RESULTS

A. Bandstructure and absorption spectra

In zigzag nanoribbons, the nanoribbon translational unit cell length is $L = a = 2.49\,\text{Å}$ and the nanoribbon width is $W = (N_{ab} - 1)\frac{\sqrt{3}}{2}a$. We consider in detail a zigzag nanoribbon with 7 dimers per translational unit cell (7 zGNR). In this case $N_{ab} = 7$ and the width of the ribbon is $W = 12.94\,\text{Å}$. The presence of the edges in the nanoribbon qualitatively alters the electronic and optical properties.

The computed bandstructure $E_n(k)$ and density of electronic states DOS(E) for π bands in 7 zGNR nanoribbons is shown in Fig. 2(a) and (b). The Brillouin zone is one dimensional with $|k| \leq \pi/L$. There are total of $2N_{ab}$ or fourteen bands. The seven bands with negative energy ($E_n(k) < 0$) are the valence bands and the seven bands with positive energy are the conduction bands. From Fig. 2(a) we note that the conduction and valence bands are asymmetric about $E = 0$. This comes from the

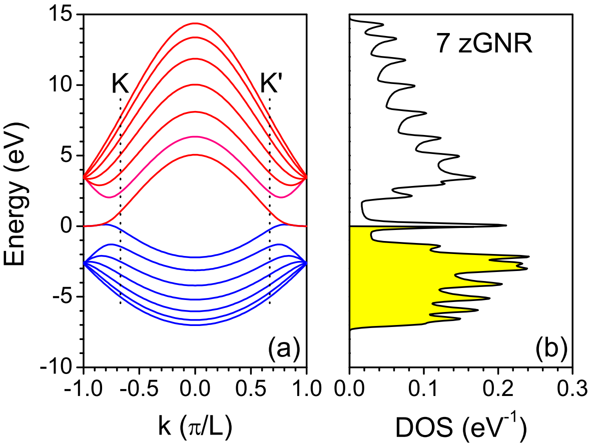

FIG. 2: (color online) (a) Computed ETB electronic bands for π electrons in a zigzag nanoribbon with 7 atoms per translational unit cell. (b) Corresponding electronic density of states. The density of states per carbon atom for the valence bands are shaded in yellow.

atomic overlap matrix elements in the ETB formalism which is not present in the simple effective mass model. We see a strong degeneracy in the bands at $k = \pm\,\pi/L$ and note that there are two partially degenerate bands near $E = 0$. These bands correspond to localized edge states for $|k| \gtrsim 2\pi/3L$ where $k = \pm\,2\pi/3L$ are the Dirac points K and K'. For $|k| \lesssim 2\pi/3L$ the states penetrate into the interior of the ribbon as $|k| \to 0$. These edge states are peculiar to zigzag nanoribbons and have been studied using effective mass, tight-binding and *ab initio* theories.[24,30,31] The remaining bands are delocalized zone folded quantum confined bands the lowest of which have parabolic minima near the Dirac points K and K' located at $k = \pm\,2\pi/3L$. The density of states shown in Fig. 2(b) has a sharp peak near $E = 0$ due to the dispersionless localized edge bands in the vicinity of $k = \pm\,\pi/L$. As we move away from $E = 0$ the density of states contains a series of von Hove singularities at the extrema of the electronic bands. As N_{ab} increases, the density of states approaches DOS(E) in planar graphene. For large N_{ab} the edge state contribution to DOS(E) decreases as $1/N_{ab}$.[24]

The absorption spectrum is shown in Fig. 3(a) for the 7 zGNR nanoribbon. For now we assume the light is linearly polarized with the electric polarization vector parallel to the nanoribbon's length. Later we will study the in-plane polarization dependence. The nanoribbon is assumed to be undoped at a temperature of 300 K. The Fermi level E_{F} at 70.16 meV is indicated by the black dashed line in Fig. 3(b). The absorption coefficient is computed using Fermi's golden rule (Eq. (8)) assuming Lorentzian lineshapes with a FWHM of 0.2 eV. The total absorption spectrum is shown in Fig. 3(a) as a thick black line. This is a sum of contributions from several transitions. The lowest lying absorption peak at 1.65 eV, labeled V2C1, is due to transitions between the low lying second hole band V2 and the higher lying first electron band C1. This transition is indicated by a vertical arrow in Fig. 3(b) whose length is the absorption peak transition energy, *i.e.* 1.65 eV. From Fig. 3(b), we see that the V2C1 peak comes from transitions between states near the K and K' points in the Brillouin zone. The initial states are quantum confined hole states V2 and the final states are the localized electron edge states C1. A second broad absorption transition V1C2 peaking at 2 eV comes from transitions between the localized hole edge states V1 and the second quantum confined electron states C2. There is a strong peak in the absorption spectrum at 2.23 eV due to the intraband transition V3V1 between V3 quantum confined states near the K and K' points and the localized V1 hole edge states.

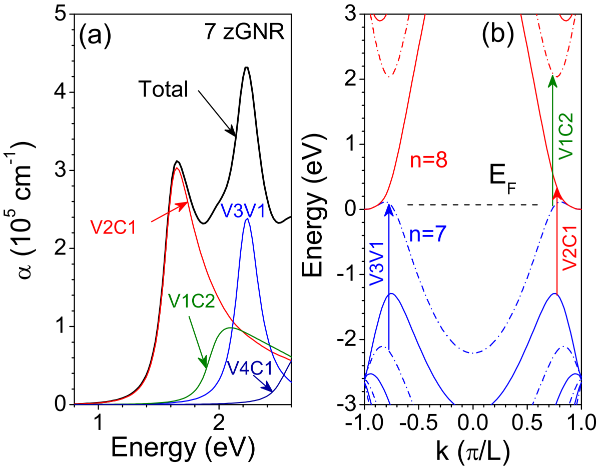

FIG. 3: (color online) (a) Band edge absorption for 7 zGNR nanoribbons with electric polarization vector parallel to the ribbon. Total absorption is the sum of absorption due to several transitions. (b) Band diagram showing the Fermi level E_{F} and transitions involved in the three lowest absorption peaks. Blue lines are valence bands and red lines are conduction bands. Solid lines (n even) are even parity states and the dash-dotted lines (n odd) are odd parity states.

The absorption spectrum in the 7 zGNR nanoribbon is qualitatively different from the absorption spectrum seen in nanotubes. A mirror plane runs down the center of the nanoribbon so the electronic states are either symmetric or antisymmetric about the mirror plane. The bands with even parity in Fig. 3(b) are solid lines and the odd parity bands are shown as dash-dotted lines. The allowed transitions for light polarized parallel to the nanoribbon axis are between bands with the same parity. In particular the interband $\Delta n = 0$ selection rule which holds for nanotubes does not hold for nanoribbons. These conclusions are in agreement with results obtained within the effective mass formalism.[32] The edge states play an im-

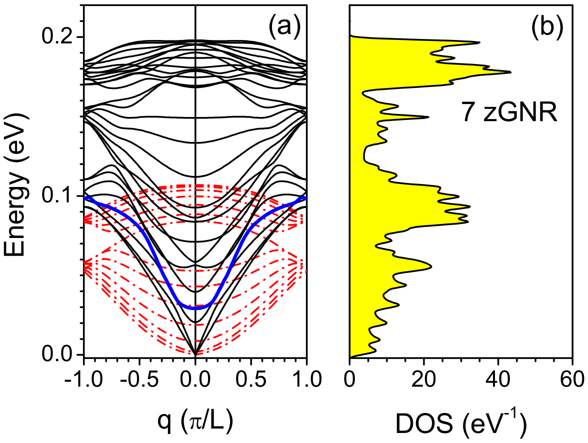

FIG. 4: (color online) (a) Phonon dispersion relations for a 7 zGNR nanoribbon calculated in the valence force field model. The out-of-plane modes are red dash-dotted lines while the remainder are in-plane modes. The band associated with the $q = 0$ RBLM mode is shown as a thick blue line. (b) Density of modes per carbon atom for the dispersion relations in (a).

portant role in the band edge transitions and the absorption spectrum is sensitive to the position of the Fermi level. In Fig. 3(b) we see that the V1 edge states in the vicinity of the Dirac points lie above the Fermi energy. Since these states are empty, electrons in the lower bands can be photoexcited into these V1 states and this accounts for the strong intraband V3V1 absorption peak seen at 2.23 eV.

Optical selection rules and absorption in zigzag nanoribbons have been studied by other authors using nearest-neighbor tight-binding approaches.[32,33] They neglect overlap matrix elements so that the conduction and valence bands are symmetric about $E = 0$. For symmetric valence and conduction bands the absorption peaks V1C2 and V2C1 are degenerate which disagrees with what we find taking overlap matrix elements into account. Our edge state bands V1 and C1 are not completely dispersionless and in undoped 7 zGNR nanoribbons we find E_{F} lies below the V1 band for a range of k values in the Brillouin zone. This gives rise to a strong V3V1 absorption feature which is not predicted in Refs. 32 and 33.

B. Phonon dispersion relations

Phonon dispersion relations for a 7 zGNR nanoribbon obtained in our valence force field (VFF) model is shown in Fig. 4(a). The dispersion relations and normal mode displacements are obtained by solving the dynamical matrix eigenvalue problem.[21] Since the force constant tensor is block diagonal, the in-plane and out-of-plane modes can be treated independently. There are 2 $N_{ab} = 14$ out-of-plane modes and these are shown as red dash-dotted lines. We find that for normally incident pump pulses, none of these out-of-plane modes can be coherently excited and so they are not of interest to us. The remaining 4 $N_{ab} = 28$ modes are in-plane modes and are shown as solid lines. We find that $N_{ab} = 7$ of the in-plane $q = 0$ modes can be coherently excited. We focus our attention on the lowest lying of these modes, the so-called radial breathing like mode (RBLM). The RBLM mode is a stretching mode in which the width of the nanoribbon breathes in and out and is somewhat analogous to the radial breathing mode (RBM) seen in nanotubes. The band associated with the RBLM is shown in Fig. 4(a) as a thick blue line. The phonon energy of the RBLM coherent phonons is $\hbar\omega = 29$ meV which corresponds to an oscillation period of 0.141 ps. The density of phonon modes is shown in Fig. 4(b). Apart from numerous von-Hove singularities, the density of phonon states in Fig. 4(b) resembles the density of phonon states in bulk graphene.[21]

The RBLM phonon energies in zGNR nanoribbons obtained from our VFF model can be fit to $\hbar\omega = AW^P + B$ where W is the zigzag nanoribbon width in Angstroms and $\hbar\omega$ is the $q = 0$ RBLM phonon energy in eV. The fitting parameters $A = 0.25247$, $P = -0.82773$ and $B = -0.00136$ are obtained from a least squares fit to our VFF results for $3 \le N_{ab} \le 15$ corresponding to widths in the range $4\,\text{Å} < W < 30\,\text{Å}$.

C. Generation of coherent phonons

In a typical simulation, we excite coherent RBLM phonons with a 20 fs Gaussian laser pulse. In our simulations the fluence F is taken to be 5×10^4 J/cm^2 and the pump pulse is linearly polarized with the electric polarization vector parallel to the nanoribbon length. The pump photon energy is 2.24 eV which coincides to the V3V1 absorption peak shown in Fig. 3(a). The pump energy density $u(t)$ is plotted against the left axis of Fig. 5(b) and the photoexcited carrier density per unit length is plotted against the right axis. The time dependent distribution functions and photogenerated carrier density are obtained by integrating the photogeneration rates in Eq. (3) using the equilibrium distribution functions as initial conditions. In integrating this equation, we assume a FWHM pump spectral width of $\Gamma_p = 150$ meV which appears in the broadened delta function. Using the time-dependent distribution functions, the RBLM coherent phonon driving function $S(t)$ can be obtained from Eq. (2). The driving function in our example is shown in Fig. 5(a). It initially rises sharply during the pump phase and reaches a peak value $S_{\max} = 94.6$ ps^{-2}. Given $S(t)$ we can solve Eq. (1) to obtain the RBLM coherent phonon amplitude $Q(t)$. Positive $Q(t)$ for the RBLM mode corresponds to an expansion of the nanoribbon width while negative $Q(t)$ corresponds to a contraction. For coherent RBLM phonon os-

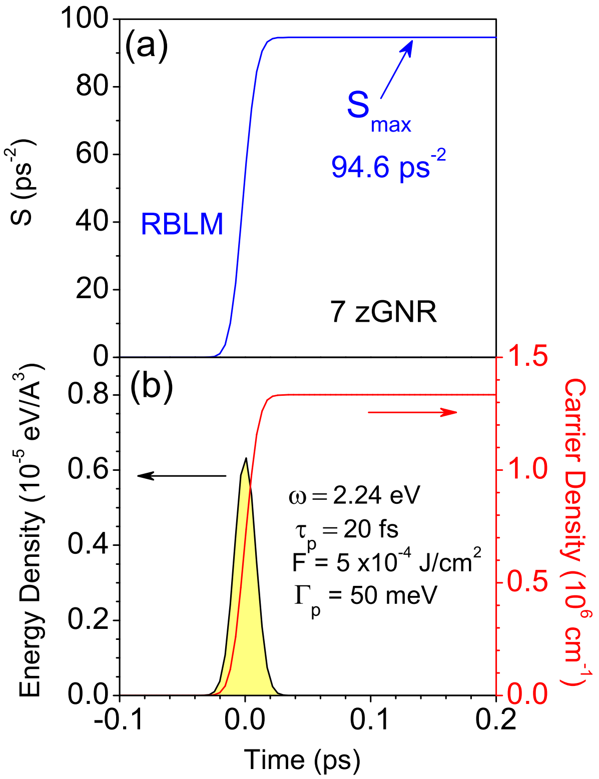

FIG. 5: (color online) For 7 zGNR nanoribbon excited by Gaussian laser pulse with polarization vector parallel to ribbon length we plot (a) coherent RBLM phonon driving function $S(t)$ and (b) pump photon energy density (left axis) and photogenerated carrier density (right axis). For the assumed pump pulse, the photon energy ω, fluence F, pulse duration τ_p, and FWHM spectral linewidth Γ_p are indicated in (b).

cillations the nanoribbon width initially expands or contracts depending on whether $S_{\max}$ is positive or negative.

Carrier scattering effects can also effect the strength of the coherent phonon oscillations especially if the scattering times are short compared to the oscillation period. A detailed treatment of carrier scattering is beyond the scope of this article. However, we note that carrier scattering by itself does not necessarily lead to a change in the driving function $S_m(t)$. According to Eq. 2, scattering affects $S_m(t)$ *only if* the carrier scatters to a state that has a *substantially different* carrier-phonon matrix element. For instance, in GaAs, an electron scattering *within* the conduction band (either via incoherent phonons or electron-electron scattering) does not change the driving function since the electron-phonon matrix elements are similar within the conduction band. We would expect that in graphene nanoribbons, scattering *within* a given band would have less of an effect than scattering *between* different bands.

We can estimate the effects of carrier dynamics on these results using a simple relaxation time approximation model for recombination of photogenerated carriers. We considered relaxation times ranging from 10 fs to 2 ps and our results are shown in Fig. 6. After an initial sharp rise due to photoexcitation by the pump, $S(t)$ decays exponentially at long times due to carrier relaxation as seen in Fig. 6(b). We then solved the driven oscillator equation (Eq. 1) for the coherent phonon amplitude $Q(t)$. In Fig. 6(a) we plot $Q(t)$ assuming a relaxation times of 10 fs (solid red curve) and in the relaxationless limit (dashed blue curve).

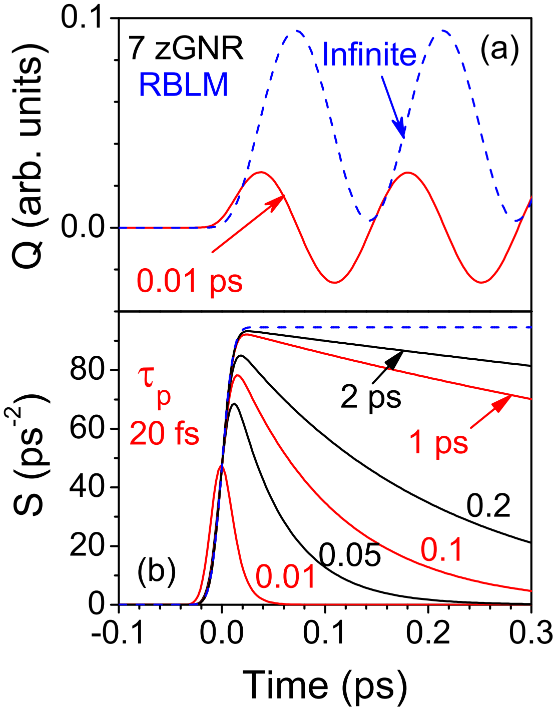

FIG. 6: (color online) For 7 zGNR nanoribbon excited by a 20 fs Gaussian laser pulse with polarization vector parallel to ribbon length we plot (b) coherent RBLM phonon driving function $S(t)$ for several relaxation times. Solid curves are labeled with the relaxation time measured in picoseconds. The dashed blue curve is the relaxationless limit. In (a) the dashed blue curve shows the coherent phonon amplitude $Q(t)$ in the relaxationless limit and the solid red curve shows $Q(t)$ assuming a 10 fs carrier relaxation time.

We note that there is a shift in phase of about $\pi/2$ between the two cases. For the 10 fs carrier relaxation time, we get a sinusoidal oscillation, while for the no relaxation case, we find that $Q(t) \propto 1 - cos(\omega t)$. These are the limiting cases for a driving function that is proportional to a delta function and a step function respectively. This is discussed in more detail in Ref. 34.

The CP signal is proportional to the square of the amplitude of the $Q(t)$ oscillations, so to estimate the effect carrier relaxation has on the computed RBLM CP signal, we solved the driven oscillator equation and found the amplitude of $Q(t)$ at long times as a function of the

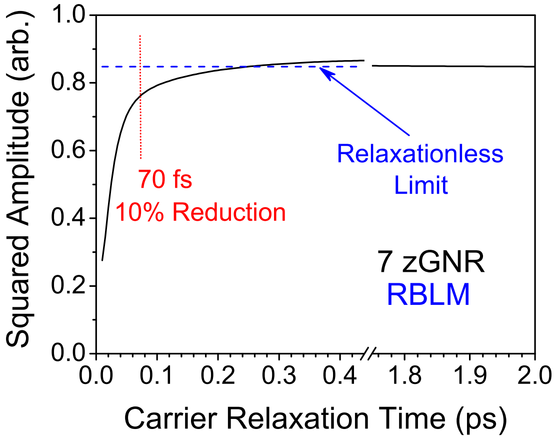

FIG. 7: (color online) For 7 zGNR nanoribbon excited by Gaussian laser pulse with polarization vector parallel to ribbon length we plot the squared RBLM coherent phonon amplitude $Q(t)^2$ as a function of carrier relaxation time. The relaxationless limit is shown as a blue dashed line for comparison. For a relaxation time of 70 fs the squared amplitude $Q(t)^2$ is reduced by 10%.

carrier relaxation time. The square of $Q(t)$ is shown in Fig. 7. We find that for relaxation times greater than 200 fs, we recover the results obtained in the absence of carrier relaxation. This is not surprising since the RBLM period is 141 fs and the point about which $Q(t)$ oscillates is able to follow slow changes in $S(t)$ adiabatically while the amplitude of the $Q(t)$ oscillations at long times remains unchanged. For relaxation times less than the RBLM period, the amplitude of $Q(t)$ at long times decreases, but even for relaxation times slightly less than the RBLM period the errors are not too great. For a relaxation time of 70 fs, we see that the square of the $Q(t)$ oscillation amplitude and hence the CP intensity is only reduced by 10%. Since 70 fs is the shortest photoexcited carrier relaxation time measured in the pump-probe experiments by Dawlaty *et al.*[27] on graphene samples, we feel that our neglect of carrier relaxation effects is a fair approximation. Henceforth, we will neglect the effects of carrier relaxation for simplicity.

Since coherent phonon spectroscopy gives direct phase information on the coherent phonon amplitude, it is instructive to examine $S_{\rm max}$ as a function of pump photon energy. This is done in Fig. 8. Fig. 8(a) is the power spectrum of $Q(t)$ at the RBLM frequency. In Fig. 8(b) we plot $S_{\rm max}$ as a function of pump photon energy. For comparison, the absorption coefficient is plotted in Fig. 8(c). Near the band edge, we see from Fig. 8(b) that the pump light is strongly absorbed at the V2C1 and V3V1 peaks. The resulting increase in the photoexcited carrier density increases the coherent phonon driving function and enhances the coherent phonon oscillation amplitudes. In other words the coherent phonon driving function near the band edge is determined by the strength of optical absorption between the lowest few hole bands and the localized edge states V1 and C1. At energies above 3 eV, $S_{\rm max}$ changes sign and the nanoribbon initially contracts.

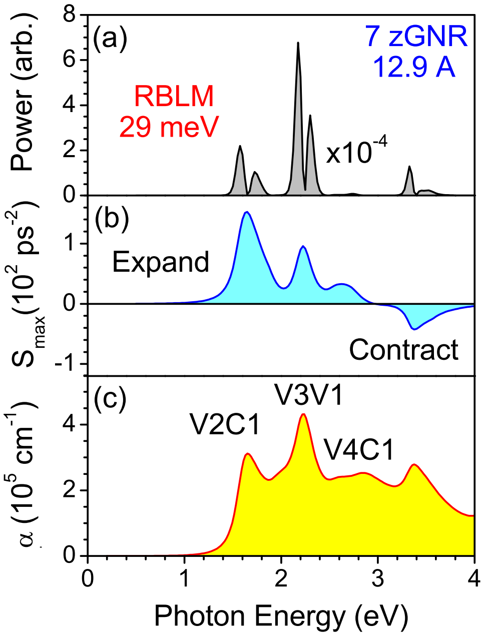

FIG. 8: (color online) For 7 zGNR nanoribbon excited by Gaussian a laser pulse with polarization vector parallel to ribbon length, we plot (a) the coherent phonon power at the RBLM frequency (29 meV), (b) the value of $S_{\rm max}$, and (c) the initial absorption spectrum as a function of photon energy.

D. Detection of coherent phonons

The generation of coherent phonons in zGNR nanoribbons results in macroscopic oscillations of the carbon atoms. The time-dependent macroscopic displacement of each carbon atom can be described as a sum of terms each of which is proportional to a different coherent phonon amplitude.[5] These displacements in turn modulate the optical properties of the nanoribbon through changes induced in the electronic band structure.

We illustrate our results in Fig. 9 where we simulate the results of a hypothetical two-color pump probe experiment on a 7 zGNR nanoribbon. As usual the fluence is 5×10^4 J/cm^2 and we assume the pump and probe are both linearly polarized with electric polarization vector parallel to the nanoribbon length. As indicated in Fig. 9(a) the pump photon energy is 2.24 eV which coincides with the peak in the V3V1 absorption feature. The time-resolved differential gain measured by the probe is given by

$$\Delta g(\hbar\omega, t) = -\left(\alpha(\hbar\omega, t) - \alpha(\hbar\omega, t \to -\infty)\right) \qquad (10)$$

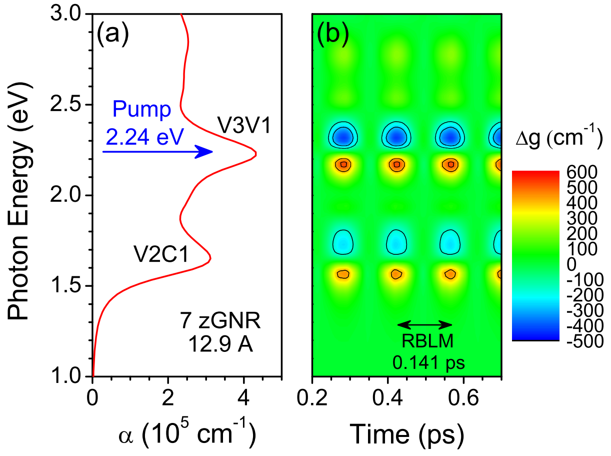

FIG. 9: (color online) For 7 zGNR nanoribbon excited by Gaussian laser pulse with polarization vector parallel to ribbon length, we plot (a) absorption coefficient as function of photon energy and (b) differential gain as a function of time and photon energy after the transient pump pulse dies out. The pump photon energy is taken to be 2.24 eV

where $\alpha(\hbar\omega, t)$ is the time dependent absorption coefficient defined in Eq. (8). The differential gain is shown in Fig. 9(b) as a function of probe delay and probe photon energy. There are large differential gain oscillations near the V2C1 and V3V1 absorption peaks which oscillate at the RBLM period of 0.141 ps, so it is clear that the dominant contribution to the time-dependent differential gain comes from RBLM induced absorption modulation. We find that the ribbon width initially expands and begins oscillating about a new and wider equilibrium width $W_0 + \Delta W$ where W_0 is the initial width before photoexcitation. When the laser pulse duration is much less than the coherent phonon period, the ribbon width oscillates between W_0 and $W_0 + 2\ \Delta W$. When the ribbon width $W(t) = W_0$ the differential gain vanishes. When $W(t) = W_0 + 2\ \Delta W$ the absorption peaks involving transitions to the localized edge states shift to higher energies giving rise to positive differential gain on the low energy side of the absorption peak and negative differential gain on the high energy side. This is clearly seen in Fig. 9(b).

The experiments we model are degenerate pump/probe measurements (i.e. the pump and probe have the same wavelength) and the pump and probe excitation energy is scanned. After background subtraction, the time-dependent differential transmission is Fourier transformed to obtain the power spectrum. Peaks in this power spectrum occur at the coherent phonon frequencies. Plotting the power spectrum at the RBLM frequency as a a function of pump/probe photon energy gives us the RBLM CP power spectrum. The RBLM CP power spectrum is shown in Fig. 8(a) as a function of pump/probe photon energy. We see strong double peaks in the RBLM CP spectra corresponding to the V2C1 and V3V1 transitions. Integrating the area under these double peaks, we obtain the RBLM CP intensity for each transition.

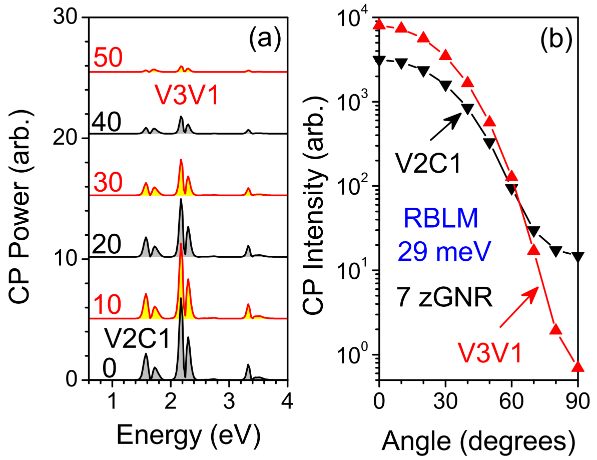

FIG. 10: (color online) For 7 zGNR excited by Gaussian laser pulse with the pump/probe polarization vector rotated an angle from the nanoribbon axis, we plot (a) the RBLM CP spectrum as a function of pump/probe energy for several polarization angles from 0 the 50 degrees and (b) the integrated RBLM CP intensity for V2C1 and V3V1 transitions.

We also investigated the in-plane polarization dependence of the coherent phonon spectra. Here the polarization of the electric field of both the pump and probe pulse are rotated by an angle θ with respect to the nanoribbon length. The dependence of the RBLM CP power spectrum on pump/probe polarization angle is shown in Fig. 10(a) where the CP power spectra are shown for polarization angles between 0 and 50 degrees. At a polarization angle of 0 degrees, there is a strong V3V1 signal at 2.25 eV and a weaker V2C1 signal at 1.65 eV. As the polarization angle increases from 0 degrees to 50 degrees, the CP signal becomes weaker. The CP intensity is plotted on a log scale in Fig. 10(b) for the V2C1 and V3V1 transitions. As the polarization angle varies from 0 to 90 degrees, the CP intensity is strongly quenched.

It is useful to plot the CP intensity as a function of nanoribbon width. We fix the pump and probe electric polarization vectors to be parallel to the nanoribbon width as this is the polarization for which the CP intensity is greatest. In Fig. 11(a), the RBLM CP intensity for the V2C1 and V3V1 transitions as a function of the number of carbon dimers in the zigzag nanoribbon unit cell is plotted against the left axis and the RBLM frequency is plotted against the right axis. In Fig. 11(b), we plot the coherent driving function amplitude $S_{\max}$ as a function of N_{ab} for the V2C1 and C3V1 transitions. We have studied all zGNR nanoribbons for N_{ab} ranging from 6 to 17 and find similar results. The driving function is positive for low energies (up to just below 3 eV)

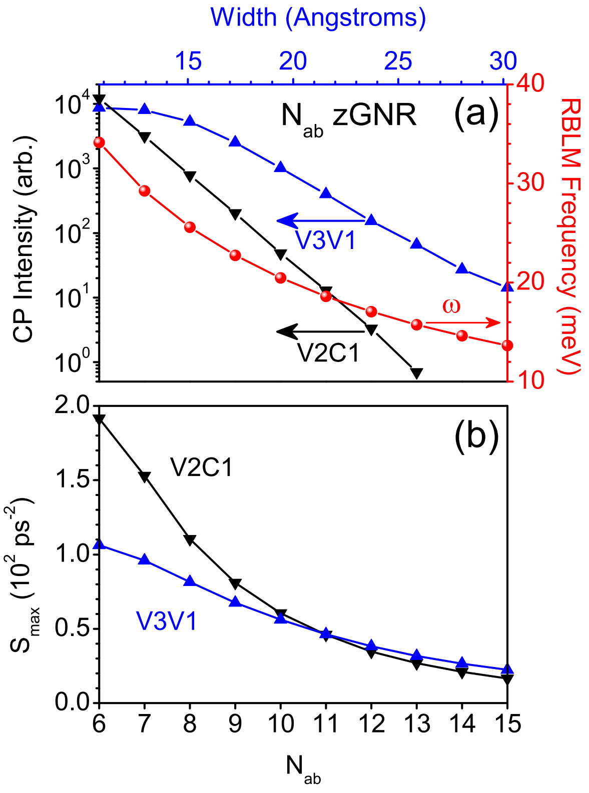

FIG. 11: (color online) For zigzag nanoribbons excited by Gaussian laser pulse with pump and probe polarization vector parallel to ribbon length, in (a) we plot the RBLM CP intensity for the V2C1 and V3V1 transitions as a function of N_{ab}, the number of carbon dimers in the zigzag unit cell, on the left axis. On the right axis in we plot the RBLM frequency ω in eV. In (b) we plot S_{max} for the V2C1 and V3V1 transitions. The ribbon width for each value of N_{ab} can be read from the upper axis.

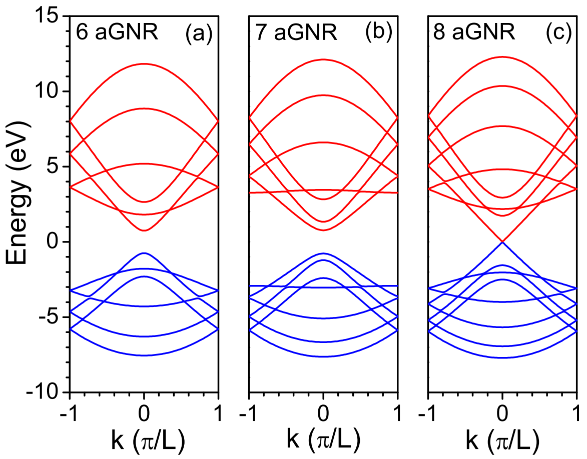

FIG. 12: (color online) Electronic band structure for three armchair nanoribbons obtained from the ETB model. We have one representative from each mod(N_{ab},3) armchair nanoribbon family: (a) 6 β-aGNR mod 0 semiconducting nanoribbon, (b) 7 γ-aGNR mod 1 semiconducting nanoribbon, and (c) 8 α-aGNR mod 2 metallic nanoribbon.

and then becomes negative for all cases.

IV. ARMCHAIR NANORIBBON RESULTS

A. Bandstructure and absorption spectra

In armchair nanoribbons (aGNR), the nanoribbon translational unit cell length is $L = \sqrt{3}\ a = 4.31$ Å and the nanoribbon width is $W = (N_{ab} - 1)\,\frac{a}{2}$. Armchair nanoribbons belong to one of three families depending on the mod number $p = \mathrm{mod}(N_{ab}, 3)$.[25,35] Following the convention of Refs. 25 and 35 we label the armchair nanoribbons as α-aGNR, β-aGNR, and γ-aGNR families for mod 2, mod 0, and mod 1 nanoribbons respectively.

Example bandstructure calculations for each nanoribbon family are shown in Fig. 12. In our ETB model, all armchair nanoribbons have a direct gap at $k = 0$. From the 6 β-aGNR mod 0 and 7 γ-aGNR mod 1 nanoribbon bands in Fig. 12(a) and (b) we see that β- and γ-aGNR ribbons are semiconducting with parabolic bands near the band edge. From the 7 α-aGNR nanoribbon band in Fig. 12(c) we see that the α-aGNR ribbons have negligible band gaps and a linear band edge dispersion relation. Unlike the case in zigzag nanoribbons, there are no localized edge states near the band edge. Armchair nanoribbons have direct gaps that arise from quantum confinement and edge effects and all the electronic wavefunctions near the band edge are distributed throughout the width of the ribbon.

In Fig. 13 we plot the direct band gap E_g in the ETB model as a function of N_{ab}, or equivalently the ribbon width W, for the α, β, and γ armchair nanoribbon families. In the case of the α-GNR family, the band gap is multiplied by a factor of 10 for clarity. We find that α-aGNRs have a small band gap that decreases with ribbon width. The β- and γ-aGNRs have large band gaps that decrease as a function of ribbon width, but they fall on different curves as seen in the figure. Our ETB results are in decent agreement with first principles results reported in Ref. 25. These results differ from simple tight binding (STB) theory which predicts that band gaps in α-aGNRs vanish identically and that band gaps for β- and γ-aGNRs as a function of ribbon width fall on the same curve.[25]. For each family, we fit the band gaps to an expression of the form $E_g = A/(W + B)$ where W is the ribbon width in Angstroms and E_g is the band gap in eV. For wide ribbons $E_g \approx A/W$. For the range $6\,\text{Å} < W < 25\,\text{Å}$, fitting parameters for each family are obtained. For α-aGNRs A = 0.486 eV-Å and B = 3.014 Å, for β-aGNRs A = 13.8 eV-Å and B = 2.082

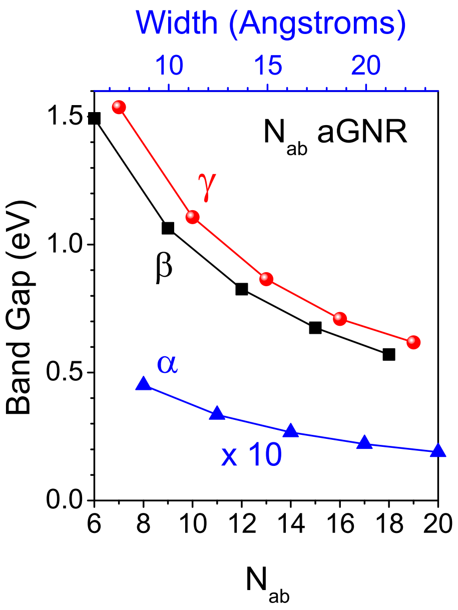

FIG. 13: (color online) Direct band gaps for armchair nanoribbons in the ETB model as a function of the number of dimers N_{ab} in the translational unit cell. Band gaps are shown for α-aGNR mod 2, β-aGNR mod 0, and γ-aGNR mod 1 families. The band gaps for the α-aGNR mod 2 nanoribbons have been multiplied by a factor of 10 for clarity. The nanoribbon width is plotted on the top axis.

Å, and for γ-aGNRs A = 14.97 eV- Å and B = 2.286 Å. These results are similar to those obtained in Ref. 35 using a semiempirical extended Hückel theory. The armchair nanoribbon band gaps in Ref. 35 are described by $E_g = A/W$ where values of A are 0.4, 8.6, and 10.4 eV- Å for α- β- and γ-aGNRs respectively.

Since there are three distinct armchair nanoribbon families α, β and γ, we've computed room temperature ($T = 300$ K) absorption spectra for an undoped nanoribbon in each family as a function of photon energy for light with electric polarization vectors parallel to the ribbon length. In computing the absorption coefficient using Fermi's golden rule (Eq. (8)) we assume Lorentzian lineshapes with the same 0.2 eV FWHM used in Fig. 3.

In Fig. 14(a) we plot the absorption spectrum in an undoped 6 β-aGNR mod 0 semiconducting nanoribbon for light polarized parallel to the nanoribbon length. The total absorption spectrum, shown as a solid black line, is a sum of absorption spectra due to three major interband direct transitions labeled E_{11}, E_{22} and E_{33}. These transitions are shown in the band diagram in the right panel of Fig. 14(a). The sharp peaks in the spectra are due to von Hove singularities at each of the transition band edges. The room temperature Fermi level is $E_{\mathrm{F}} = -29.5$ meV. The Fermi level is shifted slightly to the valence band edge since the conduction and valence bands are asymmetric in the ETB model. Sasaki *et al.*[32] have studied optical selection rules in armchair nanoribbons and find that for light polarized parallel to the nanoribbon length, the allowed interband transitions are direct transitions between valence band i and conduction band i. In order to conform to a widely used convention in the literature, the transitions in Fig. 14(a) are labeled E_{ii} as opposed to the ViCi notation used in Section III. We see that the optical selection rules in armchair nanoribbons are qualitatively different from those in zigzag nanoribbons where direct transitions are *forbidden* for polarization parallel to the ribbon.[32,33]

In Fig. 14(b) we show similar results for an undoped 7 γ-aGNR mod 1 semiconducting nanoribbon. Again the total absorption spectrum is the sum of absorption spectra due to three interband direct transitions E_{11}, E_{22} and E_{33} and the room temperature Fermi level $E_{\mathrm{F}} = -32.7$ meV is shifted slightly towards the valence band edge.

In Fig. 14(c) we show results for an undoped 8 α-aGNR mod 2 metallic nanoribbon. In the left panel of Fig. 14(c) we plot the absorption spectrum for light polarized parallel to the nanoribbon length. The total absorption spectrum, shown as a solid black line, is a sum of absorption spectra due to three major interband direct transitions labeled E_{11}, E_{22} and E_{33}. In the metallic armchair nanoribbons, we follow convention and label optical transitions starting with the lowest one defined as E_{11}. For clarity, transition energies are sometimes labeled E_{ii}^{s} or E_{ii}^{m} in semiconducting and metallic nanoribbons, respectively. Our notation should cause no confusion since it is clear from the context whether we are talking about semiconducting or metallic nanoribbons. From the band diagram in Fig. 14(c) we see that E_{11} corresponds to a direct transition between the second electron and hole bands. Optical transitions between the first electron and hole bands with linear dispersion don't contribute to the absorption spectrum. They do, however, pin the Fermi level as a function of T at $E_{\mathrm{F}} = 0$ meV as can be seen in Fig. 14(c).

B. Phonon dispersion relations

Phonon dispersion relations for 6 β-aGNR mod 0, 7 γ-aGNR mod 1, and 8 α-aGNR mod 2 nanoribbons obtained in our VFF model are shown in Figs. 15(a), (b) and (c), respectively. As in the zigzag nanoribbon case, dispersion relations and normal mode displacements are obtained by solving the dynamical matrix eigenvalue problem. The in-plane and out-of-plane modes can again be treated independently. There are 2 N_{ab} out-of-plane modes (red dash-dotted lines) and 4 N_{ab} in-plane modes (black solid lines). In all cases, we find that N_{ab} of the in-plane $q = 0$ modes can be coherently excited. The lowest of these modes is an RBLM mode. The RBLM phonon dispersion relations are shown in Fig. 15 as thick blue lines.

The $q = 0$ RBLM phonon energies in aGNR nanorib-

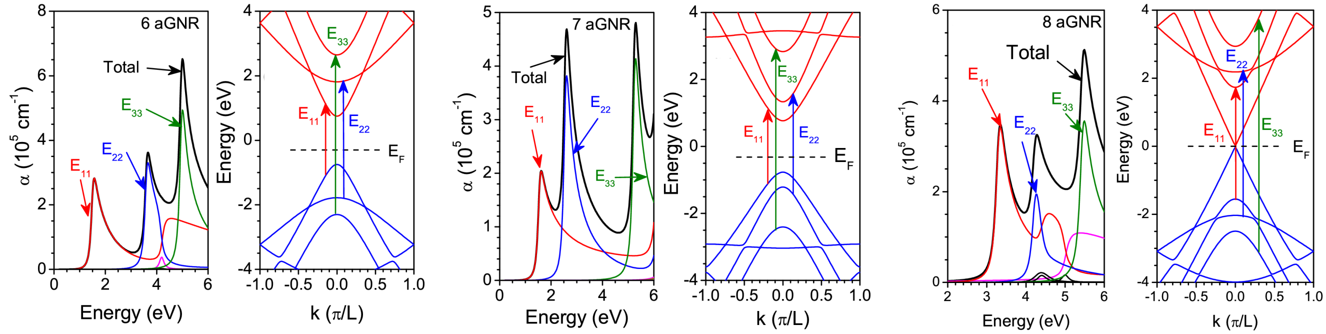

(a) (b) (c)

FIG. 14: (color online) Band absorptions with electric polarization vector parallel to the ribbon and band diagram showing the room temperature Fermi level E_{F} with transitions involved in the three lowest absorption peaks for (a) 6 β-aGNR mod 0 nanoribbon, (b) 7 γ-aGNR mod 1 nanoribbon, and (c) 8 α-aGNR mod 2 nanoribbon. Total absorption is the sum of absorption due to several transitions. In the band diagrams, blue lines are valence bands and red lines are conduction bands.

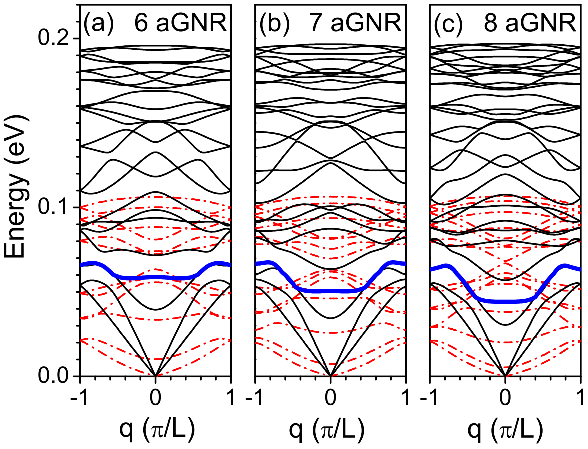

FIG. 15: (color online) Phonon dispersion relations for aGNR nanoribbons calculated in the valence force field model for (a) 6 β-aGNR mod 0, (b) 7 γ-aGNR mod 1, and (c) 8 α-aGNR mod 2 nanoribbons. The out-of-plane modes are red dash-dotted lines while the remainder are in-plane modes. The dispersion band associated with the $q = 0$ RBLM mode is shown as a thick blue line.

bons obtained from our VFF model can be fit to $\hbar\omega = AW^{P} + B$ where W is the armchir nanoribbon width in Angstroms and $\hbar\omega$ is the $q = 0$ RBLM phonon energy in eV. The fitting parameters $A = 0.31376$, $P = -0.95579$ and $B = 0.00328$ are obtained from a least squares fit to our VFF results for $4 \leq N_{ab} \leq 25$ corresponding to widths in the range $4\,\text{Å} < W < 30\,\text{Å}$.

C. Generation of coherent phonons

In our simulation, we excite coherent RBLM phonons with a 20 fs Gaussian laser pulse. The fluence F is 5×10^{4} J/cm^{2} and the pump and probe pulse are linearly polarized with an electric polarization vector parallel to the nanoribbon length. Time dependent distribution functions are obtained by integrating the photogeneration rates in Eq. (3) using the equilibrium distribution functions as initial conditions. We assume a FWHM pump spectral width of 50 meV which appears in the broadened delta function in Eq. (3). Using the time-dependent distribution functions, the RBLM coherent phonon driving function $S(t)$ can be obtained from Eq. (2).

We examine $S_{\max}$ as a function of pump photon energy and our results for 6 β-aGNR mod 0 semiconducting nanoribbons are shown in Fig. 16(a) where $S_{\max}$ is shown as a function of pump photon energy. For comparison, the absorption coefficient is also plotted in the lower panel of Fig. 16(a).

Near the band edge, we see from Fig. 16(a) that the pump light is strongly absorbed near the E_{11} and E_{22} peaks. The resulting increase in the photoexcited carrier density increases the coherent phonon driving function and enhances the coherent phonon oscillation amplitudes. Photoexcitation by the pump causes the nanoribbon to initially expand for pump photon energies near the E_{11} transition and to initially contract for pump photon energies near the E_{22} transition. We find this to be true for all β-aGNR mod 0 semiconducting nanoribbons.

Qualitatively different results are obtained for γ-aGNR mod 1 nanoribbons. In Fig. 16(b) we plot $S_{\max}$ as a function of pump photon energy for a 7 γ-aGNR mod 1 nanoribbon and find that photoexcitation by the pump causes the nanoribbon to initially contract for photon energies near the E_{11} peak and initially expand for photon energies near the E_{22} peak. This is found to be true for all γ-aGNR mod 1 semiconducting nanoribbons.

In Fig. 16(c) we show results for an 8 α-aGNR mod 2 metallic nanoribbon excited by a laser pulse polarized parallel to the ribbon length. From Fig. 16(c), we see that photoexcitation by the pump causes the nanorib-

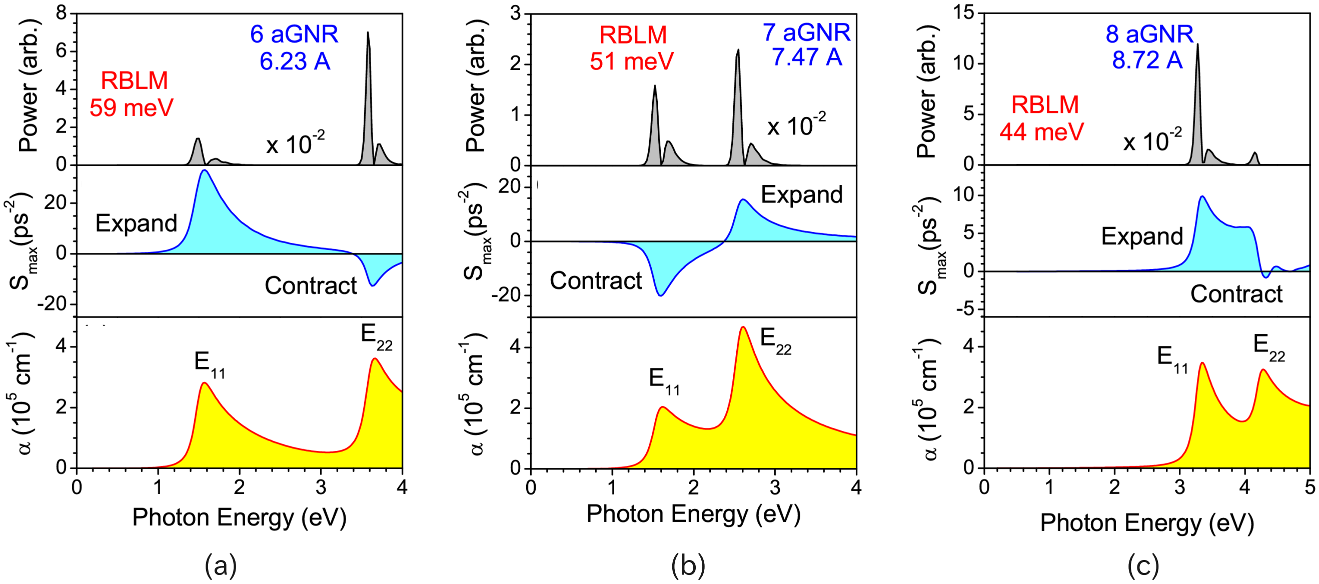

FIG. 16: (color online) The coherent phonon power, the value of $S_{\max}$, and the initial absorption spectrum are plotted as a function of photon energy for (a) 6 β-aGNR mod 0 nanoribbon (RBLM frequency = 59 meV) , (b) 7 γ-aGNR mod 1 nanoribbon (RBLM frequency = 51 meV), and (c) 8 α-aGNR mod 2 nanoribbon (RBLM frequency = 44 meV). The excitation is due to a Gaussian laser pulse with pump and probe polarization vectors parallel to the ribbon length

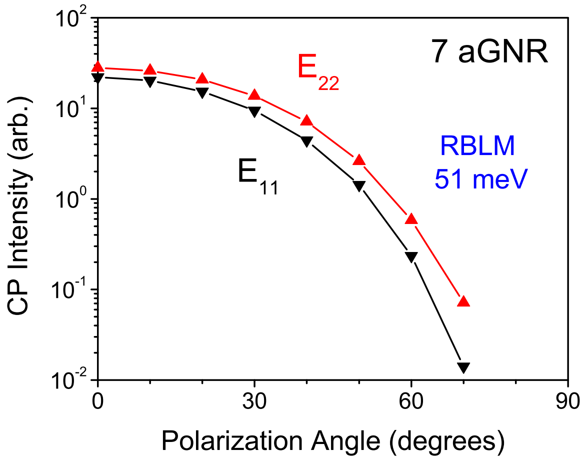

FIG. 17: (color online) Integrated RBLM CP intensity for E_{11} and E_{22} transitions excited by a Gaussian laser pulse as a function of pump/probe polarization angle in a 7 γ-aGNR mod 1 nanoribbon.

bon to initially expand for photon energies near the E_{11} transition. For photon energies near the E_{22} transition, the situation is more ambiguous.

We have studied the CP intensity for ultrafast photoexcitation near the E_{11} and E_{22} transitions in a 7 γ-aGNR mod 1 semiconducting nanoribbon as a function of polarization angle. In our simulation, we assume the polarization of pump and probe are parallel with the pump/probe polarization angle making an angle θ with the nanoribbon axis. Our results are shown in Fig. 17 and we can see that CP intensity for the E_{11} and E_{22} features in 7 γ-aGNR mod 1 semiconducting nanoribbons drop off sharply as a function of polarization angle.

We simulated CP intensity as a function of N_{ab} in armchair nanoribbons photoexcited by ultrafast Gaussian laser pulses polarized parallel to the nanoribbon length. The results are shown in Fig. 18(a) for the E_{11} and E_{22} features in α-, β-, and γ-aGNR nanoribbons. The corresponding values of the coherent phonon driving functions S_{max} are shown in Fig. 18(b).

V. ANALYSIS OF THE ELECTRON-PHONON INTERACTION

Following our previous study,[9] in this section we examine the k-dependent electron-phonon interaction in the effective mass approximation to explain why some GNRs start their coherent RBLM oscillations by initially expanding while others start the oscillations by initially shrinking. In the present discussion we will focus our attention on the aGNRs, in which we can directly use the wavefunctions formulated in previous papers.[9,36] In the case of zGNRs, we have to consider a special localized wavefunction due to the presence of edge states at which the E_{ii} transition occurs.[37] Using such a wavefunction, we obtain a constant electron-phonon matrix element that does not depend on $\mod(N_{ab}, 3)$ of the zGNRs, and thus is consistent with our results in Sec. III.

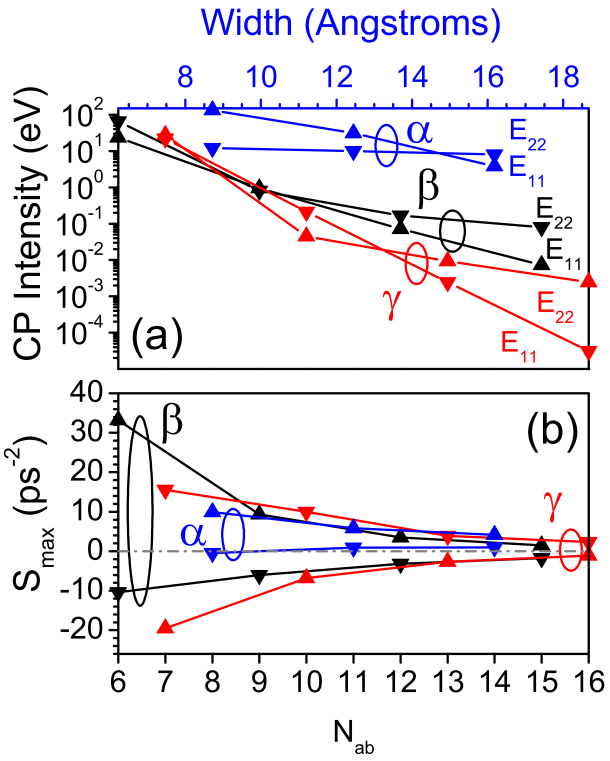

FIG. 18: (color online) For α-, β-, and γ-aGNR nanoribbons excited by Gaussian laser pulses with polarization vector parallel to ribbon length, we plot (a) RBLM CP intensity for E_{11} and E_{22} transitions and (b) the corresponding coherent phonon driving functions S_{max} as functions of N_{ab}, the number of carbon dimers in the zigzag unit cell. The curves with upward pointing arrows are for the E_{11} transitions and the downward pointing arrows are for the E_{22} transitions. The ribbon width for each value of N_{ab} can be read from the upper axis.

The details will be presented elsewhere.

The electron-phonon matrix element M_{ep} is a sum of conduction band (c) and valence band (v) electron-phonon matrix elements, which represent the electron and hole contributions, respectively,

$$\begin{aligned} M_{\mathrm{ep}} &= M_{\mathrm{ep}}^{\mathrm{c}} - M_{\mathrm{ep}}^{\mathrm{v}} \\ &= \langle \mathrm{c}|H_{\mathrm{ep}}|\mathrm{c}\rangle - \langle \mathrm{v}|H_{\mathrm{ep}}|\mathrm{v}\rangle, \end{aligned} \tag{11}$$

where H_{ep} is the GNR electron-phonon interaction Hamiltonian and the minus sign comes from the opposite charges of electrons and holes. In a nearest-neighbor effective mass approximation, the RBLM H_{ep} for an aGNR can be written as

$$H_{\mathrm{ep}} = u_{\mathrm{arm}} \begin{pmatrix} g_{\mathrm{on}} & -\frac{g_{\mathrm{off}}}{2} \\ -\frac{g_{\mathrm{off}}}{2} & g_{\mathrm{on}} \end{pmatrix}, \tag{12}$$

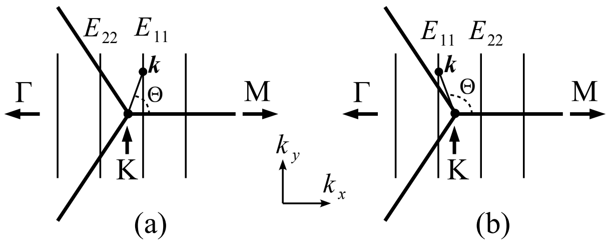

FIG. 19: Cutting lines for (a) mod 0 β-aGNR and (b) mod 1 γ-aGNRs near the Dirac K point. To make clear the definition of $\Theta(\mathbf{k})$, in this figure $\Theta(\mathbf{k})$ is shown for an arbitrary $\mathbf{k}$ at E_{11}. In fact, in the case of mod 0 and mod 1 aGNRs the E_{11} transitions occur at $\Theta(\mathbf{k}) = 0$ and $\Theta(\mathbf{k}) = \pi$, respectively. The difference between the mod 0 and mod 1 aGNRs can be understood from the position of the E_{11} or E_{22} cutting lines relative to the K point.

where g_{on} (g_{off}) is the on-site (off-site) coupling constant in eV, while u_{arm} is a ribbon width- or N_{ab}-dependent phonon amplitude. See Appendix D for the derivation of this Hamiltonian. Next, to obtain M_{ep} in Eq. (11), we use the following wavefunctions,[36]

$$\Psi_{\mathrm{c}} = \frac{\mathrm{e}^{\mathrm{i}\mathbf{k}\cdot\mathbf{r}}}{\sqrt{2S}} \begin{pmatrix} \mathrm{e}^{-\mathrm{i}\Theta(\mathbf{k})/2} \\ \mathrm{e}^{+\mathrm{i}\Theta(\mathbf{k})/2} \end{pmatrix}, \Psi_{\mathrm{v}} = \frac{\mathrm{e}^{\mathrm{i}\mathbf{k}\cdot\mathbf{r}}}{\sqrt{2S}} \begin{pmatrix} \mathrm{e}^{-\mathrm{i}\Theta(\mathbf{k})/2} \\ -\mathrm{e}^{+\mathrm{i}\Theta(\mathbf{k})/2} \end{pmatrix}, \tag{13}$$

for conduction and valence states, respectively. In Eq. (13), S is the surface area of graphene and $\Theta(\mathbf{k})$ is an angle of $\mathbf{k} = (k_x, k_y)$ measured from the k_x-axis (ribbon width direction). These wavefunctions are suitable near the graphene Dirac K point and thus they can explain well the aGNR lattice response especially at relatively low energy E_{11} and E_{22} optical transitions.

By inserting the wavefunctions in Eq. (13) into Eq. (11), we obtain

$$\langle \mathrm{c}|H_{\mathrm{ep}}|\mathrm{c}\rangle = u_{\mathrm{arm}} \left(2g_{\mathrm{on}} - g_{\mathrm{off}} \cos\Theta(\mathbf{k})\right), \tag{14a}$$

$$\langle \mathrm{v}|H_{\mathrm{ep}}|\mathrm{v}\rangle = u_{\mathrm{arm}} \left(2g_{\mathrm{on}} + g_{\mathrm{off}} \cos\Theta(\mathbf{k})\right), \tag{14b}$$

and thus

$$M_{\mathrm{ep}} = u_{\mathrm{arm}} \left(-2g_{\mathrm{off}} \cos\Theta(\mathbf{k})\right). \tag{15}$$

From this equation, we can analyze the N_{ab} and E_{ii} dependence of the aGNR initial lattice response. First of all, we should note that g_{off} (which is usually taken to be 6.4 eV as mentioned in Ref. 9) and u_{arm} (cf. Eq. (D6)) are always positive, while $\cos\Theta(\mathbf{k})$ can either be positive or negative depending on the value of $\mathbf{k}$ at which the E_{ii} transition occurs.

According to the definition of the driving force in Eqs. (1) and (2), a negative (positive) M_{ep} value corresponds to a positive (negative) S_{max}. Therefore, a positive (negative) $\cos\Theta(\mathbf{k})$ is related to a contraction (expansion) of the ribbon width. Using this argument, we can classify the aGNR lattice response based on the aGNR types. For example, let us consider semiconducting mod 0 β-aGNR and mod 1 γ-aGNRs. The cutting line position for their E_{11} and E_{22} optical transitions are just opposite to each other. For a mod 0 β-aGNR, we see

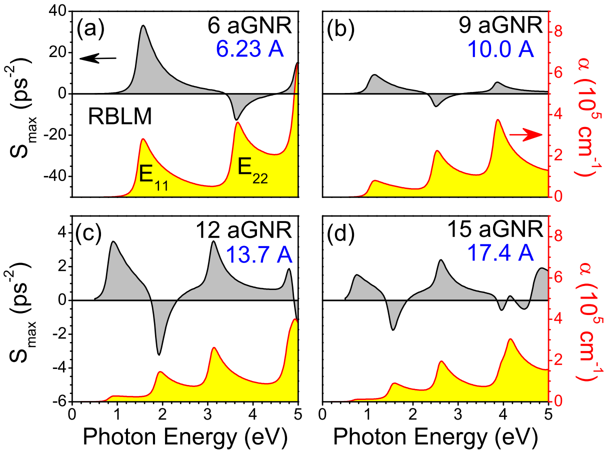

FIG. 20: (color online) Driving force $S_{\rm max}$ and initial absorption spectrum as a function of photon energy for several mod 0 semiconducting β-aGNRs: (a) $N_{ab} = 6$, (b) $N_{ab} = 9$, (c) $N_{ab} = 12$, and (d) $N_{ab} = 15$. Positive (negative) $S_{\rm max}$ at E_{11} (E_{22}) corresponds to an expansion (contraction) of the ribbon width. $\delta E = E_{22} - E_{11}$ is also shown, which is decreasing as a function of N_{ab}.

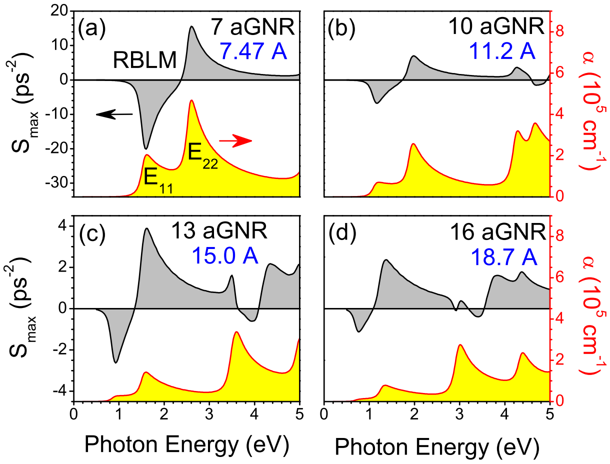

FIG. 21: (color online) Driving force $S_{\rm max}$ and initial absorption spectrum as a function of photon energy for several mod 1 semiconducting γ-aGNRs: (a) $N_{ab} = 7$, (b) $N_{ab} = 10$, (c) $N_{ab} = 13$, and (d) $N_{ab} = 16$. Negative (positive) $S_{\rm max}$ at E_{11} (E_{22}) corresponds to a contraction (expansion) of the ribbon width.

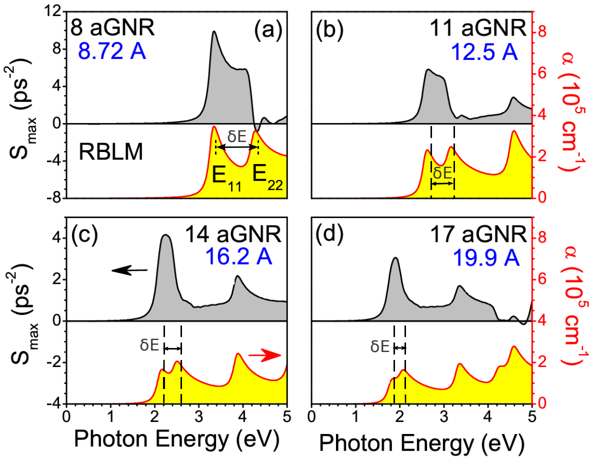

FIG. 22: (color online) Driving force $S_{\rm max}$ and initial absorption spectrum as a function of photon energy for several mod 2 metallic aGNRs: (a) $N_{ab} = 8$, (b) $N_{ab} = 11$, (c) $N_{ab} = 14$, and (d) $N_{ab} = 17$. Positive (negative) $S_{\rm max}$ at E_{11} (E_{22}) corresponds to an expansion (contraction) of the ribbon width.

that $\cos\Theta(\mathbf{k})$ becomes positive (negative) at E_{11} (E_{22}), and thus the aGNR starts the coherent phonon oscillations by expanding (shrinking) its width. This can be seen in the illustration of $\Theta(\mathbf{k})$ in Fig. 19. The opposite behavior is true for mod 1 γ-aGNRs. These arguments are consistent with our numerical results in Figs. 20 and 21, in which we show the aGNR driving force trends within the mod 0 β family and mod 1 γ family, respectively.

However, the driving force trends for the mod 2 metallic α-aGNRs (see Fig. 22) cannot be explained nicely by the effective mass theory for several reasons. The main reason is that, in the metallic α-aGNRs, there are two cutting lines with the same distance from the K point, which can be assigned as the lower and higher branches of an E_{ii} transition. Both branches contribute to a specific E_{ii} and thus we have to sum up the matrix elements from each contribution to obtain $M_{\rm ep}$. For example, if the 1D k-points for the lower and higher branches of E_{ii} are the same, the matrix elements will cancel each other because $\cos\Theta(\mathbf{k})+\cos(\pi-\Theta(\mathbf{k})) = 0$. In this case, the CP amplitude will be generally small for the mod 2 metallic aGNRs compared to the mod 0 or mod 1 semiconducting aGNRs. In the real case, we always have slightly different k-points for the lower and higher branches due to the trigonal warping effect,[38] from which the nonzero $M_{\rm ep}$ value gives information about an expansion or contraction of the ribbon width.

Near the E_{11} transition, the metallic α-aGNR initial lattice response is always an expansion for all N_{ab}. On the other hand, near the E_{22} transition, the response is expected to be always a contraction, though we see in Figs. 22 (b)-(d) the trends is not true for larger N_{ab}. We notice that the difference $\delta_E = E_{22} - E_{11}$ might determine whether or not the lattice response at the E_{22} feature of a given mod 2 N_{ab} α-aGNRs will clearly follow our effective mass theory. We guess that if δ_E is large enough ($\approx 2\,$eV as in the 8 α-aGNR), the lattice response at E_{22} should not be ambiguous. However, δ_E decreases with increasing N_{ab} as can be understood from a cutting line

TABLE I: Initial lattice behavior due to coherent phonon oscillations at E_{11} and E_{22} in aGNRs.

family	E_{11}	E_{22}
mod 0	expand	contract
mod 1	contract	expand
mod 2	expand	expand or contract

argument[39]. Thus the lattice response at E_{22} for the larger mod 2 aGNRs becomes opposite to that for the smaller mod 2 aGNRs (e.g. $N_{ab} = 2, 5, 8$).

We should also note that the E_{11} and E_{22} values of the metallic α-aGNRs are close to the order of E_{33} and E_{44} values for the semiconducting aGNRs. This gives another reason why the effective mass theory cannot explain the metallic α-aGNR trends. In this energy region, the nearest-neighbor effective mass theory should be extended to include longer-range nearest-neighbor interactions,[36] which is beyond the scope of this paper. Nevertheless, the present discussion on the effective mass theory has already given physical insight for explaining the initial lattice response of mod 0 and mod 1 semiconducting aGNRs. Even in the case of mod 2 metallic α-aGNRs we can see that the effective mass theory is still able to explain the lattice behavior near the E_{11} region. Finally, we summarize the lattice behavior at E_{11} and E_{22} transitions for all families of aGNRs in Table I.

VI. SUMMARY

We have developed a microscopic theory for the generation and detection of coherent phonons in graphene nanoribbons using an extended tight-binding model for the electronic states and a valence force field model for the phonons. We consider zigzag and armchair ribbons denoted N_{ab} zGNR and N_{ab} aGNR, respectively, where N_{ab} is the number of AB carbon dimers in the translational unit cell. In coherent phonon spectroscopy, ultrafast laser pulses generate electrons and holes in the conduction and valence bands of a graphene nanoribbon. If the pulse duration is less than the phonon oscillation period, the photogenerated carriers couple to the phonons through the deformation potential electron-phonon interaction and the nanoribbon lattice undergoes coherent macroscopic phonon oscillations. The coherent phonon amplitudes satisfy a driven oscillator equation (derived from the Heisenberg equation) with a driving function that depends on the electron-phonon interaction matrix elements and the photoexcited carrier distribution functions. For large laser spot sizes, only $q = 0$ phonon modes can be coherently excited and these modes are said to be CP active. Coherent phonons are detected using a delayed probe pulse to measure the time dependent oscillations in the differential transmission. Taking the Fourier transform of the differential transmission with respect to probe delay time, we obtain the coherent phonon spectrum as a function of phonon frequency with peaks in the CP spectrum corresponding to excited coherent phonon modes.

For both zGNRs and aGNRs there are N_{ab} CP active modes that vibrate in the plane of the nanoribbon. In all cases, the CP active mode with the lowest frequency is the RBLM mode. For 20 fs Gaussian laser pulses we ignore carrier relaxation effects and integrate Eq. (3), the photogeneration rate obtained from Fermi's golden rule, to obtain the photoexcited carrier distribution functions. Using these carrier distribution functions we obtain the driving function for RBLM coherent phonons as a function of the pump photon energy and polarization angle. In all cases we find that the driving function $S_{\max}$ immediately after photoexcitation is greatest for light polarized parallel to the nanoribbon axis. For photoexcitation near the optical absorption edge, we find that the coherent phonon driving function for the RBLM mode is much larger for zigzag nanoribbons where $\Delta n \neq 0$ transitions involving localized edge states provide the dominant contribution to the CP driving function. The sign of $S_{\max}$ is interesting since it gives phase information that can be measured in CP spectroscopy. In zigzag nanoribbons, the ribbons initially expand for pump photon energies near the V2C1 and V3V1 absorption features. In armchair nanoribbons the phase behavior is different for the α, β and γ families where $\Delta n = 0$ transitions between zone folded quantum confined states give rise to the CP driving function. In β-aGNR mod 0 semiconducting aGNRs the ribbon initially expands for pumping near the E_{11} absorption peak and contracts for pumping near E_{22}. In γ-aGNR mod 1 semiconducting aGNRs the ribbon initially contracts for pumping near the E_{11} absorption peak and expands for pumping near E_{22}. In the case of the metallic α-aGNR mod 2 ribbons, the ribbon is seen to expand for pumping near the E_{11} feature while the behavior near the E_{22} feature is ambiguous. Such lattice responses are also discussed by considering the electron-phonon interaction within an effective mass theory.

Acknowledgments

This work was supported by the National Science Foundation under grant Nos. DMR-1105437 and OISE-0968405, the Office of Naval Research under grant No. ONR-00075094, R.S. acknowledges MEXT grant (Ministry of Education, Japan, No. 20241023.)

Appendix A: Electronic states in extended tight binding model

In treating electronic states in zigzag and armchair nanoribbons within the ETB model, we assume that all bond lengths and bond angles between A and B carbon atoms are the same as that in planar graphene. In addition, we assume the ribbon edges are unpassivated. Since the nanoribbons are assumed to be perfectly planar, there is no mixing of σ and π orbitals and the two types of bonds can be considered separately. The σ bonds account for the mechanical properties of the ribbon while the π bonds determine the optical properties near the band edge and play the dominant role in the generation of coherent phonons. We treat the valence π and conduction π^* bands using the third-nearest-neighbor extended tight binding (ETB) model developed by Porezag *et al.* for carbon compounds.[19] The Hamiltonian and overlap matrix elements between π orbitals on different sites are parameterized by analytic expressions that depend on the C-C bond length. These parameterizations were calibrated using DFT results for a local orbital basis set in the local density approximation (LDA) for a wide range of carbon compounds.

A graphene nanoribbon only has translational symmetry along its length with period L so the Brillouin zone is one dimensional with a wavevector k satisfying $|k| \leq \pi/L$. The tight binding wavefunction for a π electron with wavevector k is given by

$$\psi_k(\mathbf{r}) = \sum_{s=A}^{B} \sum_{j=1}^{N_{ab}} C_{sj}(k) \sum_{l=-\infty}^{\infty} e^{i(kL)l} \ \phi_\pi(\mathbf{r} - \mathbf{R}^l_{sj}) \quad \text{(A1)}$$

where $\phi_\pi(\mathbf{r})$ are atomic $2p_z$ orbitals, $\mathbf{R}^l_{sj}$ is the position of carbon atom sj in the l-th translational unit cell.

The tight binding expansion coefficients $C_{sj}(k)$ in Eq. (A1) satisfy the generalized eigenvalue equation

$$\sum_{s'j'} H^{ss'}_{jj'}(k) \ C_{s'j'}(k) = E(k) \sum_{s'j'} S^{ss'}_{jj'}(k) \ C_{s'j'}(k). \quad \text{(A2)}$$

The Hamiltonian matrix elements are given by

$$H^{ss'}_{jj'}(k) = \sum_{l} e^{i(kL)l} \ H^{CC}_{pp\pi} \left(\left| \mathbf{R}^l_{s'j'} - \mathbf{R}^0_{s'j'} \right| \right), \quad \text{(A3)}$$

where $H^{CC}_{pp\pi}(d)$ is the Hamiltonian matrix element between two carbon $2p_z$ π orbitals as a function of the distance d between them. A similar expression holds for $S^{ss'}_{jj'}(k)$ with $H^{CC}_{pp\pi}(d)$ replaced by the overlap matrix element $S^{CC}_{pp\pi}(d)$. The ETB matrix elements vanish at a finite cutoff distance, and the sum over l in Eq. (A3) includes all contributions out to third nearest neighbor shells. Analytic expressions for $H^{CC}_{pp\pi}$ and $S^{CC}_{pp\pi}$ can be found in Ref. 19.

Solving Eq. (A2) we obtain the electronic states $E_n(k)$ and wavefunctions where $n = 1 \ldots 2N_{ab}$ is the subband index in order of increasing energy. The first N_{ab} levels are the valence bands and the remainder are conduction bands.

Appendix B: Phonon modes in valence force field model

We treat lattice dynamics in zigzag and armchair nanoribbons using a Born-von Karman valence force field model.[20,21,40] We let $\mathbf{U}^l_{sj}(t)$ be the displacement from equilibrium of a carbon atom at $\mathbf{R}^l_{sj}$. The equations of motion are given by

$$\frac{d\mathbf{U}^l_{sj}(t)}{dt} = \sum_{s'j'l'} \mathbf{K}_{sjl;s'j'l'} \left(\mathbf{U}^{l'}_{s'j'}(t) - \mathbf{U}^l_{sj}(t) \right). \quad \text{(B1)}$$

The force constant tensor $\mathbf{K}_{sjl;s'j'l'}$ depends on the distance between atoms sjl the $s'j'l'$. In order to describe bond twisting interactions involving four atoms it is necessary to retain up to fourth nearest neighbor shell force constant tensors. If η labels nearest neighbor shells and d_η is the distance between them, the force constant tensor connecting η-th neighbor atoms is

$$\mathbf{K}_{sjl;s'j'l'} = \begin{pmatrix} \phi^\eta_r \tau_x^2 + \phi^\eta_{ti} \tau_y^2 & (\phi^\eta_{ti} - \phi^\eta_r)\tau_x \tau_y & 0 \\ (\phi^\eta_{ti} - \phi^\eta_r)\tau_x \tau_y & \phi^\eta_r \tau_y^2 + \phi^\eta_{ti} \tau_x^2 & 0 \\ 0 & 0 & \phi^\eta_{to} \end{pmatrix}, \quad \text{(B2)}$$

where ϕ^η_r is the η-th neighbor force constant parameter in the radial bond-stretching direction and ϕ^η_{ti} and ϕ^η_{to} are η-th neighbor force constants for the transverse in-plane and out-of-plane directions. For neighbor shells $\eta = 1 \ldots 4$, we use the force constants tabulated in Table I of Ref. 21 and reproduced in Table 9.1 of Ref. 20. The vector τ is a vector of unit length from atom sjl to $s'j'l'$.

Taking the Fourier transform of the atomic displacements, we obtain

$$\mathbf{U}^l_{sj}(t) = \frac{1}{\sqrt{N_\Omega}} \sum_{\mathbf{q}} \mathbf{U}_{sj}(q) \ e^{-i\mathbf{q}\cdot\mathbf{R}^l_{sj}} \quad \text{(B3)}$$

where $\mathbf{U}_{sj}(q)$ are the normal mode displacement vectors and $\mathbf{q}$ is parallel to the nanoribbon axis. The phonon energies and mode displacement vectors are obtained by solving the dynamical matrix eigenvalue problem

$$\sum_{s'j'} \mathbf{D}_{sj;s'j'}(q) \ \mathbf{U}_{s'j'}(q) = M\omega(q)^2 \ \mathbf{U}_{sj}(q), \quad \text{(B4)}$$

where M is the carbon atom mass and $\omega(q)$ is the eigenfrequency of the phonon mode. In terms of the force constant tensor, the dynamical matrix is given by

$$\begin{aligned} \mathbf{D}_{sj;s'j'}(q) &= \delta_{ss'}\delta_{jj'} \sum_{s''j''l''} \mathbf{K}_{sj0;s''j''l''} \\ &\quad - \sum_{l''} \mathbf{K}_{sj0;s'j'l''} \ e^{-i\mathbf{q}\cdot\left(\mathbf{R}^{l''}_{s'j'} - \mathbf{R}^0_{sj}\right)}. \quad \text{(B5)} \end{aligned}$$

For each value of q the dynamical matrix eigenvalue problem can be solved to obtain phonon energies $\hbar\omega_m(q)$ and displacement vectors $\mathbf{U}^m_{sj}(q)$ where m labels the phonon modes.

Appendix C: Electron-phonon interaction in ETB model

The second-quantized electron-phonon interaction in zigzag and armchair nanoribbons in the ETB model is obtained by evaluating the integral

$$\hat{H}_{ep} = \int d\mathbf{r}\ \hat{\psi}^\dagger(\mathbf{r})\ H_{ep}(\mathbf{r})\ \hat{\psi}(\mathbf{r}) \tag{C1}$$

where the deformation potential electron-phonon interaction Hamiltonian is

$$H_{ep}(\mathbf{r}) = -\sum_{sjl} \nabla v_c(\mathbf{r} - \mathbf{R}^l_{sj}) \cdot \mathbf{U}^l_{sj}. \tag{C2}$$

The electron field operator $\hat{\psi}(\mathbf{r})$ is

$$\hat{\psi}(\mathbf{r}) = \sum_{nk} c_{nk}\ \psi_{nk}(\mathbf{r}), \tag{C3}$$

where $\psi_{nk}(\mathbf{r})$ are the tight binding wavefunctions for wavevector k in Eq. (A1) with $n = 1 \ldots 2N_{ab}$ labeling the subband levels. The annihilation operator for this electronic state is c_{nk}.

After carrying out this integral over the electronic coordinate, we obtain the final result by replacing the classical atomic displacements $\mathbf{U}^l_{sj}$ with the second-quantized operator

$$\mathbf{U}^l_{sj} = \frac{\hbar}{\sqrt{2\rho L_\Omega}} \sum_{mq} \frac{\hat{\mathbf{e}}^m_{sj}(q)}{\sqrt{\hbar\omega_m(q)}} e^{iqLl} \left(b_{mq} + b^\dagger_{m,-q} \right). \tag{C4}$$

Here ρ is the mass density per unit length and L_Ω is the nanoribbon length. The atomic displacements $\mathbf{e}^m_{sj}(q)$ are eigenvectors of the dynamical matrix in Eq. (B5). They satisfy the normalization condition

$$\sum_{sj} \mathbf{e}^m_{sj}(q)^* \cdot \mathbf{e}^{m'}_{sj}(q) = \delta_{m,m'}. \tag{C5}$$

The final result for the second-quantized electron-phonon interaction is

$$\hat{H}_{ep} = \sum_m \sum_{n'k';nk} M^{mq}_{n'k';nk}\ c^\dagger_{n'k'} c_{nk}\ (b_{mq} + b^\dagger_{m,-q}), \tag{C6}$$

where $q \equiv k' - k$. The interaction matrix elements is given by

$$M^{mq}_{n'k';nk} = -A_m(q) \sum_{sj;s'j'} C^*_{s'j'}(n'k')\ C_{sj}(nk) \times \sum_{ll';s''j''} e^{iL(kl-k'l')}\ \hat{\mathbf{e}}^m_{s''j''}(q) \cdot \vec{\lambda}(s'j'l'; s''j''; sjl), \tag{C7}$$

where $A_m(q) = \hbar/\sqrt{2\rho L_\Omega\ \hbar\omega_m(q)}$ is the quantized phonon amplitude. In Eq. (C7) L is the length of the translational unit cell, $C_{sj}(nk)$ are the electron tight-binding expansion coefficients in Eq. (A1), $\hat{\mathbf{e}}^m_{sj}(q)$ are the atomic normal mode displacements obtained by diagonalizing the dynamical matrix in Eq. (B5), and $\vec{\lambda}$ is the deformation potential vector.

The deformation potential vector is the three center integral

$$\vec{\lambda} = \int d\mathbf{r}\ \phi^*_\pi(\mathbf{r} - \mathbf{R}^{l'}_{s'j'})\ \nabla v(\mathbf{r} - \mathbf{R}^0_{s''j''})\ \phi_\pi(\mathbf{r} - \mathbf{R}^l_{sj}). \tag{C8}$$

We evaluate $\vec{\lambda}$ using the $2p_z$ atomic wavefunctions and screened atomic potential for carbon in Ref. 22 obtained from an *ab initio* calculation in graphene.[23] The π orbitals are expanded as

$$\phi_\pi(\mathbf{r}) = z \sum_{l=1}^{4} I_l\ \exp\left(-\frac{r^2}{2\sigma_l^2} \right), \tag{C9}$$

where the z direction is perpendicular to the nanoribbon plane. Similarly the screened atomic potentials are expanded as

$$v(\mathbf{r}) = \frac{1}{r} \sum_{l=1}^{4} v_l\ \exp\left(-\frac{r^2}{2\tau_l^2} \right). \tag{C10}$$

Values of I_l, v_l, σ_l and τ_l are tabulated in Table I of Ref. 22. Substituting the expansions (C9) and (C10) into Eq. (C8) we obtain an expansion for $\vec{\lambda}$ in terms of three-dimensional integrals which can be evaluated analytically.[22,23]

Appendix D: RBLM electron-phonon interaction in effective mass model

In this section, we derive Eq. (12) which gives the RBLM electron-phonon interaction Hamiltonian $H_{\rm ep}$ for an armchair nanoribbon. The Hamiltonian can be decomposed into the on-site and off-site Hamiltonians. The details of the on-site and off-site interactions are given in Sasaki's work on the deformation-induced gauge field in graphene.[36] We will directly use his results in formulating the on-site and off-site Hamiltonians. The on-site and off-site interactions are induced by a lattice deformation which gives rise to a change in the transfer integral and a change in the potential between A and B atoms. We adopt a coordinate system shown in Fig. 23 to derive $H_{\rm ep}$.

On-site Hamiltonian

The on-site Hamiltonian can be expressed in terms of the divergence of $\mathbf{u}_{\rm A}$ and $\mathbf{u}_{\rm B}$, which represent the displacement vector of A-atom and B-atom in the graphene unit cell, respectively. This Hamiltonian is written as

$$\mathcal{H}_{\rm on} = g_{\rm on} \begin{pmatrix} \nabla \cdot \mathbf{u}_{\rm B}(\mathbf{r}) & 0 \\ 0 & \nabla \cdot \mathbf{u}_{\rm A}(\mathbf{r}) \end{pmatrix}. \tag{D1}$$

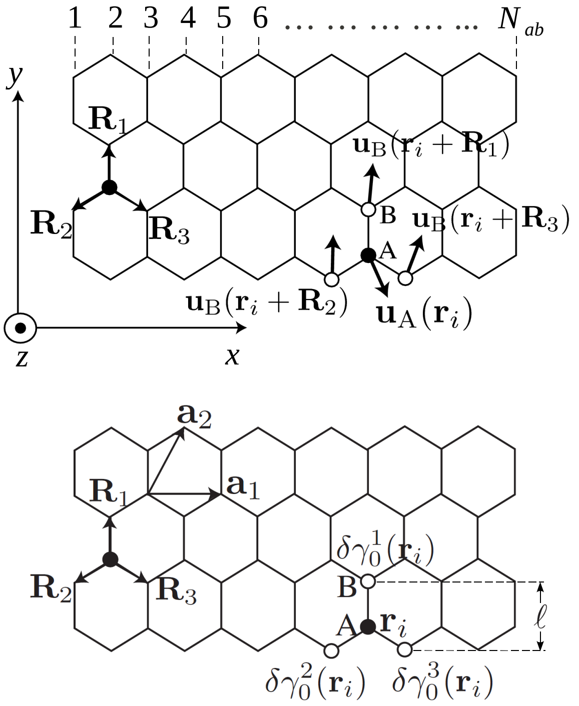
1 2 3 4 5 6 ... ... N_{ab}
y
x
z
$\mathbf{R}_1$
$\mathbf{R}_2$
$\mathbf{R}_3$
$\mathbf{u}_\mathrm{B}(\mathbf{r}_i+\mathbf{R}_1)$
B
$\mathbf{u}_\mathrm{B}(\mathbf{r}_i+\mathbf{R}_3)$
A
$\mathbf{u}_\mathrm{B}(\mathbf{r}_i+\mathbf{R}_2)$
$\mathbf{u}_\mathrm{A}(\mathbf{r}_i)$
$\mathbf{a}_2$
$\mathbf{R}_1$
$\mathbf{a}_1$
$\mathbf{R}_2$
$\mathbf{R}_3$
$\delta\gamma_0^1(\mathbf{r}_i)$
B
A
$\mathbf{r}_i$
ℓ
$\delta\gamma_0^2(\mathbf{r}_i)$
$\delta\gamma_0^3(\mathbf{r}_i)$

FIG. 23: Upper panel shows displacements of B-atoms at $\mathbf{r}_i + \mathbf{R}_a$ ($a = 1, 2, 3$), that is $\mathbf{u}_\mathrm{B}(\mathbf{r}_i + \mathbf{R}_a)$, which give rise to a deformation potential at A-atom of $\mathbf{r}_i$. Lower panel shows local modulations of the hopping integral defined by $\delta\gamma_0^a(\mathbf{r})$ ($a = 1, 2, 3$). In this coordinate system we have the nearest-neighbor vectors $\mathbf{R}_1 = (0, a_\mathrm{cc})$, $\mathbf{R}_2 = (-\sqrt{3}/2, -1/2)a_\mathrm{cc}$, $\mathbf{R}_3 = (\sqrt{3}/2, -1/2)a_\mathrm{cc}$, where $a_\mathrm{cc} = a/\sqrt{3}$. Here $\ell = 3a_\mathrm{cc}/2$ is used in Eq. (D9).

For the discussion of the RBLM electron-phonon interaction, we rewrite Eq. (D1) as follows:

$$\begin{aligned}\mathcal{H}_\mathrm{on} &= g_\mathrm{on}\sigma_0\nabla\cdot\left(\frac{\mathbf{u}_\mathrm{A}(\mathbf{r})+\mathbf{u}_\mathrm{B}(\mathbf{r})}{2}\right)\\ &+ g_\mathrm{on}\sigma_z\nabla\cdot\left(\frac{\mathbf{u}_\mathrm{A}(\mathbf{r})-\mathbf{u}_\mathrm{B}(\mathbf{r})}{2}\right),\end{aligned} \tag{D2}$$

where g_on denotes the gradient of the atomic potential at $\mathbf{r}$, σ_0 is the identity matrix, and σ_z is the z-component of the vector of Pauli matrices. For the RBLM in armchair nanoribbons we have $\mathbf{u}_\mathrm{A}(\mathbf{r}) = \mathbf{u}_\mathrm{B}(\mathbf{r}) = \mathbf{u}(\mathbf{r})$. Therefore, Eq. (D2) can be simplified to be

$$\mathcal{H}_\mathrm{on} = g_\mathrm{on}\sigma_0\nabla\cdot\mathbf{u}(\mathbf{r}). \tag{D3}$$

The RBLM oscillation can be expressed by

$$\mathbf{u}(\mathbf{r}) = u_m\sin(k_m x)\hat{\mathbf{e}}_x, \tag{D4}$$

where u_m is the maximum amplitude of the RBLM oscillation at the armchair edge. The wavevector k_m is then specified by π/W, where W is the ribbon width. By substituting $\mathbf{u}(\mathbf{r})$ in Eq. (D4) into Eq. (D3), we obtain

$$\mathcal{H}_\mathrm{on} = u_\mathrm{arm}\begin{pmatrix} g_\mathrm{on} & 0\\ 0 & g_\mathrm{on}\end{pmatrix}, \tag{D5}$$

where, for simplicity, here we have defined

$$u_\mathrm{arm}(x) = k_m u_m\cos(k_m x). \tag{D6}$$

Note that u_arm is always positive because the atomic position x is within the range $-W/2 \le x \le W/2$.

Off-site Hamiltonian

To derive the off-site interaction Hamiltonian, we start with the fact that the lattice deformation modifies the nearest-neighbor hopping integral locally as $-\gamma_0 \to -\gamma_0 + \delta\gamma_0^a(\mathbf{r}_i)$ ($a = 1, 2, 3$). The corresponding perturbation of the lattice deformation is given by

$$\mathcal{H}_\mathrm{deform} \equiv \sum_{i\in\mathrm{A}}\sum_{a=1,2,3}\delta\gamma_0^a(\mathbf{r}_i)\left[(c_{i+a}^\mathrm{B})^\dagger c_i^\mathrm{A} + (c_i^\mathrm{A})^\dagger c_{i+a}^\mathrm{B}\right], \tag{D7}$$

where c_i^A is the annihilation operator for a π electron on an A-atom at position $\mathbf{r}_i$, and $(c_{i+a}^\mathrm{B})^\dagger$ is the creation operator for a π electron on a B-atom at position $\mathbf{r}_{i+a}$ ($= \mathbf{r}_i + \mathbf{R}_a$). This perturbation gives rise to scattering within a region near the K-point of graphene whose interaction is given by a deformation-induced gauge field $\mathbf{A}(\mathbf{r}) = (A_x(\mathbf{r}), A_y(\mathbf{r}))$ as $v_\mathrm{F}\sigma\cdot[\hat{\mathbf{p}} + \mathbf{A}(\mathbf{r})]$, where v_F is the Fermi velocity, $\hat{\mathbf{p}} = -i\hbar\nabla$ is the momentum operator, and σ is the Pauli matrix. The deformation-induced gauge field $\mathbf{A}(\mathbf{r})$ is defined from $\delta\gamma_0^a(\mathbf{r})$ ($a = 1, 2, 3$) as[36]

$$\begin{aligned} v_\mathrm{F}A_x(\mathbf{r}) &= \delta\gamma_0^1(\mathbf{r}) - \frac{1}{2}\left[\delta\gamma_0^2(\mathbf{r}) + \delta\gamma_0^3(\mathbf{r})\right],\\ v_\mathrm{F}A_y(\mathbf{r}) &= \frac{\sqrt{3}}{2}\left[\delta\gamma_0^2(\mathbf{r}) - \delta\gamma_0^3(\mathbf{r})\right].\end{aligned} \tag{D8}$$

Similar to the RBM electron-phonon interaction in carbon nanotubes,[41] the perturbation to the nearest-neighbor hoppping integral for the RBLM electron phonon interaction in the armchair nanoribbons is given by

$$\delta\gamma_0^a(\mathbf{r}) = \frac{g_\mathrm{off}}{\ell a_\mathrm{cc}}\mathbf{R}_a\cdot\{\mathbf{u}(\mathbf{r}+\mathbf{R}_a) - \mathbf{u}(\mathbf{r})\}, \tag{D9}$$

where g_off is the off-site coupling constant and $\ell = 3a_\mathrm{cc}/2$ (see the lower panel of Fig. 23). Here the displacement vector of a carbon atom at $\mathbf{r}$ in general is expressed by $\mathbf{u}(\mathbf{r}) = [u_x(\mathbf{r}), u_y(\mathbf{r})]$. Using a Taylor expansion, we approximate Eq. (D9) as

$$\delta\gamma_0^a(\mathbf{r}) = \frac{g_\mathrm{off}}{\ell a_\mathrm{cc}}\mathbf{R}_a\cdot\{(\mathbf{R}_a\cdot\nabla)\mathbf{u}(\mathbf{r})\}. \tag{D10}$$

Using $\mathbf{R}_1$, $\mathbf{R}_2$, and $\mathbf{R}_3$ in Fig. 23, we obtain the deformation-induced gauge field of Eq. (D8) as follows:

$$\begin{aligned} v_{\rm F}A_x(\mathbf{r}) &= \frac{g_{\rm off}}{2}\left[-\frac{\partial u_x(\mathbf{r})}{\partial x}+\frac{\partial u_y(\mathbf{r})}{\partial y}\right], \\ v_{\rm F}A_y(\mathbf{r}) &= \frac{g_{\rm off}}{2}\left[\frac{\partial u_x(\mathbf{r})}{\partial y}+\frac{\partial u_y(\mathbf{r})}{\partial x}\right]. \end{aligned} \tag{D11}$$

Inserting $\mathbf{u}(\mathbf{r})$ in Eq. (D4) into this last equation, we then obtain

$$v_{\rm F}A_x = -\frac{g_{\rm off}}{2}k_m u_m\cos(k_m x) = -\frac{g_{\rm off}}{2}u_{\rm arm}, \tag{D12}$$

while $v_{\rm F}A_y = 0$. Therefore, the off-site Hamiltonian can be written as

$$\mathcal{H}_{\rm off} = \sigma_x v_F A_x = u_{\rm arm}\begin{pmatrix} 0 & -\frac{g_{\rm off}}{2} \\ -\frac{g_{\rm off}}{2} & 0 \end{pmatrix}. \tag{D13}$$

Finally, we can get the electron-phonon interaction Hamiltonian of Eq. (12):

$$\begin{aligned} H_{\rm ep} &= \mathcal{H}_{\rm on}+\mathcal{H}_{\rm off} \\ &= u_{\rm arm}\begin{pmatrix} g_{\rm on} & -\frac{g_{\rm off}}{2} \\ -\frac{g_{\rm off}}{2} & g_{\rm on} \end{pmatrix}. \end{aligned} \tag{D14}$$

---

[1] A. Gambetta, C. Manzoni, E. Menna, M. Meneghetti, G. Cerullo, G. Lanzani, S. Tretiak, A. Piryatinski, A. Saxena, R. L. Martin, et al., Nature Phys. **2**, 515 (2006).

[2] Y. S. Lim, K. J. Yee, J. H. Kim, E. H. Haroz, J. Shaver, J. Kono, S. K. Doorn, R. H. Hauge, and R. E. Smalley, Nano Lett. **6**, 2696 (2006).

[3] Y.-S. Lim, K.-J. Yee, J. H. Kim, E. H. Háróz, J. Shaver, J. Kono, S. K. Doorn, R. H. Hauge, and R. E. Smalley, J. Korean Phys. Soc. **51**, 306 (2007).

[4] K. Kato, K. Ishioka, M. Kitajima, J. Tang, R. Saito, and H. Petek, Nano Lett. **8**, 3102 (2008).

[5] G. D. Sanders, C. J. Stanton, J.-H. Kim, K.-J. Yee, Y.-S. Lim, E. H. Háróz, L. G. Booshehri, J. Kono, and R. Saito, Phys. Rev. B **79**, 205434 (2009).

[6] J.-H. Kim, K.-J. Han, N.-J. Kim, K.-J. Yee, Y.-S. Lim, G. D. Sanders, C. J. Stanton, L. G. Booshehri, E. H. Háróz, and J. Kono, Phys. Rev. Lett. **102**, 037402 (2009).

[7] L. G. Booshehri, C. L. Pint, G. D. Sanders, L. Ren, C. Sun, E. H. Háróz, J.-H. Kim, K.-J. Yee, Y.-S. Lim, R. H. Hauge, et al., Phys. Rev. B **83**, 195411 (2011).

[8] Y.-S. Lim, J.-G. Ahn, J.-H. Kim, K.-J. Yee, T. Joo, S.-H. Baik, E. H. Haroz, L. G. Booshehri, and J. Kono, ACS Nano **4**, 3222 (2010).

[9] A. R. T. Nugraha, G. D. Sanders, K. Sato, C. J. Stanton, M. S. Dresselhaus, and R. Saito, Phys. Rev. B **84**, 174302 (2011).

[10] P. Avouris, Z. Chen, and V. Perebeinos, Nature Nanotechnol. **2**, 605 (2007).

[11] Z. Chen, Y. M. Lin, M. J. Rooks, and P. Avouris, Physica E: Low-dimensional Systems and Nanostructures **40**, 228 (2007).

[12] A. Fasoli, A. Colli, A. Lombardo, and A. C. Ferrari, Phys. Status Solidi B **246**, 2514 (2009), ISSN 1521-3951.

[13] L. Tapaszto, G. Dobrik, P. Lambin, and L. Biro, Nature Nanotechnol. **3**, 397 (2008).

[14] J. Bai, X. Duan, and Y. Huang, Nano Lett. **9**, 2083 (2009).

[15] D. Kosynkin, A. Higginbotham, A. Sinitskii, J. Lomeda, A. Dimiev, B. Price, and J. Tour, Nature **458**, 872 (2009).

[16] J. Cai, P. Ruffieux, R. Jaafar, M. Bieri, T. Braun, S. Blankenburg, M. Muoth, A. Seitsonen, M. Saleh, X. Feng, et al., Nature **466**, 470 (2010).

[17] S. Masubuchi, M. Ono, K. Yoshida, K. Hirakawa, and T. Machida, Appl. Phys. Lett. **94**, 082107 (2009).

[18] B. Huang, Q. Yan, Z. Li, and W. Duan, Front. Phys. China **4**, 269 (2009).

[19] D. Porezag, T. Frauenheim, T. Köhler, G. Seifert, and R. Kaschner, Phys. Rev. B **51**, 12947 (1995).

[20] R. Saito, G. Dresselhaus, and M. S. Dresselhaus, *Physical Properties of Carbon Nanotubes* (Imperial College Press, London, 1998).

[21] R. Al-Jishi, L. Venkataraman, M. S. Dresselhaus, and G. Dresselhaus, Chem. Phys. Lett. **209**, 77 (1993).

[22] J. Jiang, R. Saito, G. G. Samsonidze, S. G. Chou, A. Jorio, G. Dresselhaus, and M. S. Dresselhaus, Phys. Rev. B **72**, 235408 (2005).

[23] A. Grüneis, Ph.D. thesis, Tohoku University, Sendai, Japan (2004).

[24] K. Nakada, M. Fujita, G. Dresselhaus, and M. S. Dresselhaus, Phys. Rev. B **54**, 17954 (1996).

[25] Y. W. Son, M. L. Cohen, and S. G. Louie, Phys. Rev. Lett. **97**, 216803 (2006).

[26] S. L. Chuang, *Physics of Optoelectronic Devices* (Wiley, New York, 1995).

[27] J. Dawlaty, S. Shivaraman, M. Chandrashekhar, F. Rana, and M. Spencer, Appl. Phys. Lett. **92**, 042116 (2008).

[28] F. Bassani and G. P. Parravicini, *Electronic States and Optical Transitions in Solids* (Pergamon, New York, 1975).

[29] W. H. Press, S. A. Teukolsky, W. T. Vetterling, and B. P. Flannery, *Numerical Recipes* (Cambridge University Press, New York, 1992).

[30] M. Fujita, K. Wakabayashi, K. Nakada, and K. Kusakabe, J. Phys. Soc. Jpn. **65**, 1920 (1996).

[31] L. Pisani, J. A. Chan, B. Montanari, and N. M. Harrison, Phys. Rev. B **75**, 064418 (2007).

[32] K. Sasaki, K. Kato, Y. Tokura, K. Oguri, and T. Sogawa, Phys. Rev. B **84**, 085458 (2011).

[33] H. Hsu and L. E. Reichl, Phys. Rev. B **76**, 045418 (2007).

[34] A. V. Kuznetsov and C. J. Stanton, Chapter 7: Theory of Coherent Phonon Oscillations in Bulk GaAs in *Ultrafast Phenomena in Semiconductors* (Springer-Verlag, New York, editor: Kong-Thon Tsen, 2001).

[35] H. Raza and E. C. Kan, Phys. Rev. B **77**, 245434 (2008).

[36] K. Sasaki and R. Saito, Prog. Theor. Phys. Suppl. **176**, 253 (2008).

[37] K. Sasaki, S. Murakami, and R. Saito, J. Phys. Soc. Jpn. **75**, 074713 (2006).

[38] R. Saito, G. Dresselhaus, and M. S. Dresselhaus, Phys. Rev. B **61**, 2981 (2000).

[39] K. Wakabayashi, K. Sasaki, T. Nakanishi, and T. Enoki, Sci. and Technol. Adv. Mater. **11**, 054504 (2010).

[40] R. Al-Jishi and G. Dresselhaus, Phys. Rev. B **26**, 4514 (1982).

[41] K. Sasaki, R. Saito, G. Dresselhaus, M. S. Dresselhaus, H. Farhat, and J. Kong, Phys. Rev. B **78**, 235405 (2008).